CONDUCTING FOG RESEARCH AND ABATEMENT USING UNMANNED AIRCRAFT SYSTEMS (UAS)

by

Michael Douglas Willette
Bachelor of Science, University of Northern Colorado, 2016
Bachelor of Science, Colorado State University, 2014

A Thesis

Submitted to the Graduate Faculty

of the

University of North Dakota

in partial fulfillment of the requirements

for the degree of
Master of Science

Grand Forks, North Dakota

December
2023

APPROVAL PAGE

to be completed after thesis defense

Link to form:
https://und.edu/academics/graduate-school/current-students/forms.html#d34e163--3

PERMISSION

Title	Unmanned Aircraft Systems (UAS) for Fog Research and Conducting an Operational Fog Abatement Program
Department	Atmospheric Sciences
Degree	Master of Science

In presenting this thesis in partial fulfillment of the requirements for a graduate degree from the University of North Dakota, I agree that the library of this University shall make it freely available for inspection. I further agree that permission for extensive copying for scholarly purposes may be granted by the professor who supervised my thesis work or, in his absence, by the Chairpersons of the department or the dean of the school of Graduate Studies. It is understood that due recognition shall be given to me and to the University of North Dakota in any scholarly use which may be made of any material in my thesis.

Michael Willette

TABLE OF CONTENTS

LIST OF FIGURES

LIST OF TABLES

ACKNOWLEDGEMENTS

This research is supported under a National Science Foundation RAPID grant to conduct fog measurements. Firstly, the author would like to thank Dr. David Delene for his instrumental guidance and support. The author would like to sincerely thank the licensed Unmanned Aircraft Vehecle (UAV) pilot Alex Sailsbury, Weather Modification International Incorporated, Fargo, ND, for his tireless work in procuring and operating the UAV throughout the project. The author would also like to specifically thank Dave Singewald for his initial guidance on wiring and electrical equipment, Nicholas Camp for his work during the UAV missions, and Jennifer Moore for general project support. Without any of the individuals previously listed, this project would not have been remotely as successful.

Finally, the author would like to thank his family and friends. To his family, the author expresses his upmost appreciation for their continuous love and support throughout everything life has thrown, even though we are thousands of miles apart. To his friends within the UND community, the camaraderie grown over the years will be something the author will always cherish and never forget. To his friends outside the UND community, the author expresses his gratitude for all the support and patience while working on his graduate degree.

ABSTRACT

The tremendous safety and monetary impacts of long-duration fog events continue to spur interest in its anthropogenic dissipation. With the emergence of the Unmanned Aircraft Systems (UAS) platform and the development of miniaturized atmospheric sensors, more efficient methods of fog research and anthropogenic fog dispersal may be achieved. The feasibility of a supercooled fog dispersal project in the Red River Valley and the efficacy of using the UAS platform to acquire in-situ fog microphysical data are explored. A 30-year climatology of the Red River Valley indicates increased supercooled fog potential between early November through early April, peaking in March. Five UAS missions conducted during March of 2023 demonstrate in-situ, boundary layer measurements in both high- and low-visibility conditions. The IMet-XQ2 (temperature, humidity, and location) and MiniOFS (visibility) instruments deployed on the UAS platform compare well to surface counterparts and performed sufficiently for proper representation of the atmosphere; however, aspiration of the sensors is essential for accurate measurements. The MiniOFS overestimates low-visibility events whereas the IMet-XQ2 relative humidity sensor underestimates moist atmospheres. Vertical profiling of two fog events successfully resolved the fog layers and determined fog-top heights of 114 m (375 ft) and 92 m (300 ft) AGL. During the last mission, a strong temperature inversion is present at the fog layer top. The UAS platform is deemed sufficient for in-situ data acquisition within the boundary layer; whereas a low average of 14 hours of supercooled fog per year indicate a need for additional cost effectiveness assessments for Red River Valley fog abatement feasibility.

CHAPTER I: INTRODUCTION

There is vested interest in the anthropogenic dissipation of fog. Long duration, dense fog events can induce crippling societal and economic impacts; particularly, for the aviation industry. Model-based prediction of fog remains lackluster due to computational constraints and an absence of detailed microphysical knowledge within the cloud layer. The recent emergence of unmanned aircraft systems (UAS) has resulted in an examination of how the platform could be employed for operational fog abatement projects, such as the clearing of fog near airports. In tandem with miniaturized atmospheric sensors, UAS platforms have considerable potential to revolutionize in-situ data acquisition within the boundary layer and aid in fog-related research. It is the objective of this study to determine both the feasibility of a UAS-based fog abatement project and the efficacy of the UAS-platform to obtain fog microphysical measurements within the Red River Valley of eastern North Dakota and western Minnesota.

The detrimental impact of fog on human safety and local communities is well known. According to the U.S. Department of Transportation Federal Highway Administration (2022), over 38,700 vehicle crashes occur annually due to fog, resulting in 16,300 injuries and over 600 fatalities. Kroft et al. (2003) shows that in fog-prone locations, up to 10 percent of all motor vehicle accidents are attributable to visibility reductions due to fog. Transportation (air, sea, land) economic losses due to impaired visibilities from fog can be comparable to losses from intense tornado outbreaks and wintertime blizzards (Gultepe et al. 2007). Fog-related aviation issues arise from the obscuration of runways during aircraft landings, leading to costly diversions and unsafe attempted landings. Compared to all weather-related aviation accidents, reduced visibility comprises 50 and 21 precent of accidents in Canada and United States, respectively (Gultepe et al.

2017). Of fatal weather-related aviation accidents, fog (14 %) and low ceilings (20 %) are the most prevalent factors (Capobianco and Lee 2001).

The international definition of fog constitutes an assortment of small hydrometeors (water droplets or ice crystals) suspended at the Earth's surface that reduces horizontal visibility to a minimum of 1 km (5/8 statute miles) (National Oceanic and Atmospheric Administration 2019). Although mist has a similar distinction, it has a defined visibility threshold less than 11.2 km (7 statute miles) but greater than or equal to 1 km (5/8 statute miles). Hydrometeor in fog range from 0.5 to 50 µm in diameter, with considerable variability in size distributions (Garland 1971, Gultepe et al. 2007, Liu et al. 2020). As part of the Radiation and Aerosol Cloud Experiment exploring boundary layer stratiform clouds, visibility within warm fogs was shown to be correlated with droplet concentration (N_d) and liquid water content (LWC) (Gultepe et al. 2006). The relationship is described using,

$$Vis_{fi} = \frac{1.002}{(LWC * N_d)^{0.6473}}. \qquad 1$$

where the extinction coefficient (β) is related to LWC within fogs using a power law relationship (Eldridge 1971, Kunkel 1984). However, the relationship is highly variable but can be parameterized as,

$$\beta = a(LWC)^b, \qquad 2$$

where a and b are empirically derived constants: $65 \leq a \leq 178$ and $0.63 \leq b \leq 0.96$ (Gultepe et al. 2007). Thus, various microphysical parameters (LWC, N_d) of a warm fog layer can be theoretically determined if optical parameters (Vis_{fi}, β) are measured and empiric constants are resolved.

Fog formation and life cycles are highly complex processes that are largely dependent on the microphysical and dynamical nature of the boundary layer (Stolaki et al. 2009). Formation generally occurs within broad subsidence aloft, radiative cooling at the surface, and some form of surface moisture. Evolution of the cloud layer is strongly reliant on fog top radiative cooling, maturing subsidence, and heat/moisture fluxes (Mason 1982; Gultepe et al. 2007, 2017). Groundbreaking efforts by Willett (1928) grouped eleven categories of fogs into three main types: advection fog, radiation fog, and maritime fog. Advective fogs are typically characterized by the transport of a warm and moist airmass over a thermodynamically colder surface (Liu et al. 2016). As the warm airmass cools, relative humidity increases while specific humidity remains constant, resulting in eventual condensation of the airmass (Willett 1928). Advection fog commonly occurs near coastal areas where interfaces of differing heat capacities (warmer moist ocean, cooler land) interact with favorable low-level winds. As such, true advection fogs are uncommon within intracontinental regions. Radiation fogs are defined by strong radiative cooling at the surface underneath extensive subsidence aloft, typically maximized during the early morning hours (Gultepe et al. 2007). Clear skies and a sinking stagnant airmass allow for efficient heat removal, allowing temperatures to lower to the dew point and initiate condensation of the near-surface layer. Radiation fogs favor high mountain valleys and uniform surfaces of lower heat capacities. Also known as advection-radiation fogs, maritime fogs function as a combination of radiative and advective processes, where a maritime airmass (often transitional) advects inland over a radiatively cooled land surface (Willett 1928; Gultepe et al. 2007). Advection-radiation fogs can occur along any large bodies of water, where advantageous conditions for radiative cooling interact with transitory lake/sea breezes (Ryznar 1977).

Methods to anthropogenically dissipate fog and near-surface cloudiness, are dependent on its physical characteristics and temperature. Ice fog is comprised of suspended ice crystals at, or near, the surface with temperatures less than -20 °C (Gultepe et al. 2017). Limited to high-latitude artic regions, ice fog is relatively common in the vicinity of vapor sources, such as lakes, rivers, and anthropogenic emissions (Weinstein 1977). Fog formation is generally preceded by strong radiative cooling, a subsequent formation of a robust temperature inversion, and a deep stable layer above the surface (Gultepe et al. 2015, 2017; Leung et al. 2020). Once ice crystal formation has occurred, ice fog is exceedingly difficult to disperse due to its thermodynamically stable nature (Lease and Zeigler 1972). Modification efforts via conventional aircraft downwash of drier air results in limited improvement, with successful dispersal methods relegated to preventative measures in transporting anthropogenic vapor sources (Weinstein 1977).

Warm fog consists of suspended hydrometeors along the surface at temperatures greater than the nominal freezing point of 0 °C and is the most common type of fog in the mid-latitudes. According to Weinstein (1974), in an average fog year between 0.8 to 2.0 percent of air traffic at United States airports are affected by warm fog, rising up to 40 percent at airports during record years where fog is seasonal. Warm fog dispersal can be achieved by implementing a process of physical removal (of water content) or a process of evaporation (of hydrometeors). Physical removal methods do not have much practicality outside of ephemeral entrainment-limited dispersal (airmass removal) or theoretical applications (sound waves) (Houghton and Radford 1936, Christensen and Frost 1980). On the other hand, pioneering work by Houghton and Radford (1936) has shown that evaporative methods via hygroscopic materials (salts, alkalines, urea) can be successful in mitigating visibility losses and is widely used in operational warm fog dispersal efforts (Weinstein and Silverman 1973, Park et al. 2023).

Supercooled fog is comprised of suspended liquid hydrometeors at temperatures below freezing and above -40 °C and is prominent within the Red River Valley. While simultaneously the rarest, and most dangerous type of fog, supercooled fog abatement is the easiest to remove operationally due to its metastable nature. Widely regarded as the inception of anthropogenic weather modification, the serendipitous discovery of dry ice inducing high concentrations of ice embryos by Schaefer (1946) occurred as part of collective efforts to ascertain a material to nucleate supercooled clouds. A test of this dry ice effect on supercooled ground fog instigated a conversion to snow crystals (Schaefer 1968). Shortly thereafter, Vonnegut (1947) deduced that silver iodide (AgI) acted as an effective supercooled cloud nucleant due to the close resemblance to ice crystalline structure. Based on these early discoveries, the first organized supercooled fog abatement project using conventional aircraft occurred in 1965 as part of a collective effort of airline corporations to implement clearing of airport runways and demonstrated an 80 percent success rate of visibility reductions (Beckwith 1965). Also notable, Vardiman et al. (1971) utilized ground-based generators and observed runway visibility improvements in 25 of 29 seeding operations.

Supercooled fog modification theory focuses on the injection of seeding material into a metastable system, resulting in ice crystal fallout and subsequent surface visibility improvements. Within supercooled clouds, the ambient vapor pressure falls between the higher saturation vapor pressure with respect to water and the lower saturation vapor pressure with respect to ice. Consequentially, the air is sub-saturated with respect to water, and super-saturated with respect to ice (Vardiman et al. 1971; Hoffmann 2020). As such, ice crystals have the potential to rapidly grow at the expense of supercooled water droplets via the Wengener-Bergeron-Findeison process (Korolev 2007; Storelvmo and Ivy 2015). Fog droplets can persist in a supercooled state to temperatures as cold as -40 °C in the absence of ice nucleating particles (Pruppacher and Klett 2010). Consequently, the supercooled fog modification process is contingent on the type of nucleation that initiates ice crystal growth.

As discussed by Pruppacher and Klett (2010), homogenous nucleation of supercooled water droplets occurs at temperatures below -40 °C. At this thermal threshold, the height of the free-energy barrier between phases becomes negligible; any minor fluctuation from the equilibrium state of the system instigates the formation of the lower energy, solid state (Oxtoby 1992). Therefore, supercooled fog modification methods utilizing homogeneous nucleation must thermally cool a parcel to a temperature below -40 °C to initiate ice crystal growth. Most commonly, this is accomplished through sublimation using dry ice, or by evaporation using liquified propane (Vardiman et al. 1971; Hicks and Vali 1973; Weinstein and Hicks 1976). On the other hand, heterogeneous nucleation can occur at ambient temperatures well above the -40 °C threshold required for homogenous nucleation (Lease and Zeigler 1972). At low supersaturations typically found within clouds, materials that have a good structural match with the nucleating phase and have strong interactions with the metastable phase are candidates for heterogeneous nucleation (Liu 2000). Vonnegut (1947) showed that both dimensions of the unit cell of ice and AgI are the same to within one percent, heralding AgI as the industry-standard seeding agent for weather modification methods instigating heterogeneous nucleation. Problematically, AgI effectiveness at temperatures where supercooled fog is most prevalent ($-5\ °C \leq T \leq 0\ °C$) decreases as you approach the freezing point.

With near-surface restrictions constraining conventional aircraft operations, the emergence of UAS has introduced a new platform for releasing cloud seeding agents and collection atmospheric data within the boundary layer. Figure 1 depicts an idealized small UAS supercooled fog abatement mission within the Red River Valley using an Unmanned Aircraft Vehicle (UAV). The UAV flies upwind of an airport runway and just below the top of the fog layer, releasing seeding material to initiate ice crystal growth through heterogeneous nucleation. Downwind of the injection point, ice crystals grow at the expense of supercooled water droplets until collision-coalescence processes occur and gravity-induced fallout through the entire depth of the fog commences. With enough fallout surface visibility improves, cloud-base heights rise, and cloud dispersal occurs through increasing radiative heating and turbulent mixing.

The conceptual model in Figure 1 highlights the requirements necessary for a determination of the feasibility of a supercooled fog abatement project. The UAS platform must be capable of low visibility and supercooled flight maneuvers while maintaining operational capacity. Miniaturized instrumentation attached to the UAS platform must be effective within adverse conditions, capable of efficient profiling and subsequent determination of fog top height. Surface observations can provide both confirmation and verification of changes in atmospheric conditions during operational procedures. Using the Red River Valley as the target operational area, steps to implement an operational program using the UAS platform are as follows:

1. Production of a detailed fog climatology to understand patterns of fog occurrence and extent, which provides information on operational project period(s).
2. Selecting an Unmanned Aircraft Vehicle (UAV) capable of maneuvers within low-visibility and supercooled conditions.
3. Obtain FAA-approval for operations of a UAS that can release seeding material from the surface to the top of the fog layer.
4. Produce a detailed operational plan for conducting the project; ideally, with a research component for assessing efficacy of operations.
5. Conduct an operational field project.
6. Evaluate operations.

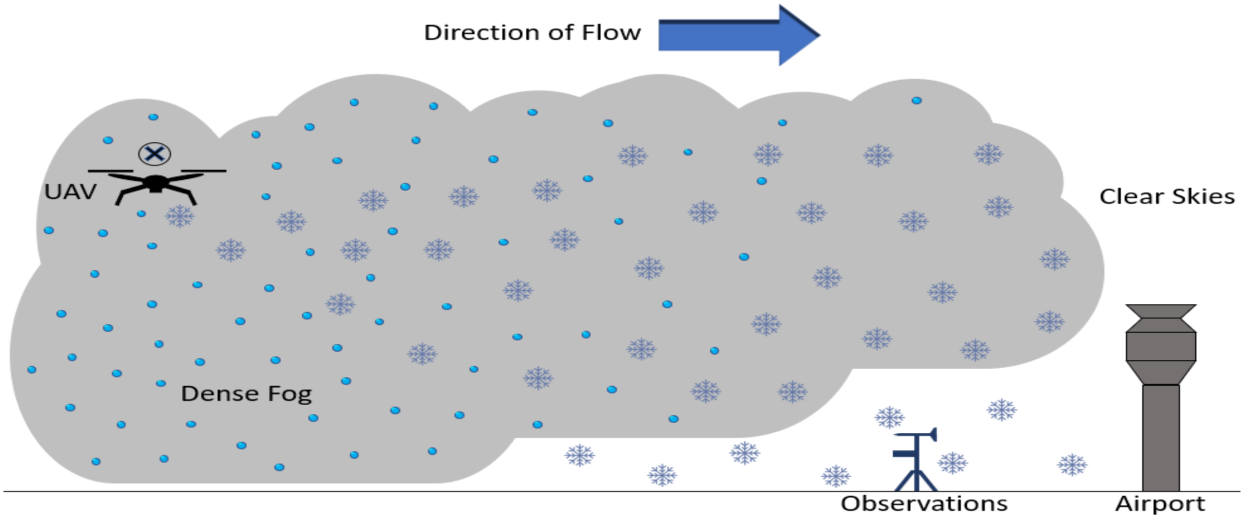

Figure 1. Image showing the conceptual model for conducting a supercooled fog dispersal project utilizing UAV technology.

CHAPTER II: INSTRUMENTATION AND DATA

IMet-XQ2

The IMet-XQ2 is a second-generation instrument for standard atmospheric parameter measurements created by International Met Systems. The IMet-XQ2 is designed to be a UAS component that provides high-resolution, boundary-layer profiles with radiosonde-quality sensors which measure temperature, relative humidity, pressure, and position (Table 1). The bead thermistor temperature sensor consists of a resistor whose resistance is strongly dependent on temperature. Proper aspiration is required for accurate measurement and efficient response times. The capacitive humidity sensor emits an electromagnetic field that is sensitive to changes in ambient relative humidity. Response time of the humidity sensor increases dramatically with decreasing temperature, particularly with temperatures below freezing. Data sampling for the IMet-XQ2 sensor package occurs every second. An internal flash drive houses fifteen hours of data capacity with a rechargeable battery life of five hours. Data can be acquired through USB serial data transmission (Raspberry Pi 4B) and through the IMet-X Control software interface.

Table 1. Table listing the IMet-XQ2 sensor specifications. Note that the response time of the temperature and relative humidity sensors are contingent on a minimum of 5 m/s of airflow. The range of response times for the humidity sensor is temperature dependent: 0.6 seconds at 25 °C, 5.2 seconds at 5 °C, and 10.9 seconds at -10 °C. Accuracy for the GPS sensor is measured in the vertical.

Measurement	Sensor	Range		Accuracy	Resolution	Response
Temperature	Bead Thermistor	-90 °C	50 °C	± 0.3 °C	0.01 °C	1.0 – 10.0 s
Humidity	Capacitive	0.0 %	100 %	± 5 %	0.1 %	0.6 - 10.9 s
Pressure	Piezoresistive	10 hPa	1200 hPa	± 1.5 hPa	0.01 hPa	0.01 s
GPS	Ublox CAM-M8	0.0 m	50,000 m	12 m (vert.)	2.5 m	1.0 s

The first generation IMet-XQ was evaluated by placing instruments at different locations on a rotary wing UAVs (Kimball et al. 2020). The precision and accuracy of the sensors was found to be best in overcast conditions (or locations with minimal direct solar radiation) when the sensors are strongly aspirated by propeller wash, displacement away from heat generated by the main electrical components (rotor arms, batteries) of the UAV, and locations upwind from the UAV body. IMet-XQ sensors attached to the front rotor arms performed best, with locations underneath the body of the UAV also deemed practical. However, sensors underneath the UAV body may be contaminated by heat from the electrical components during ascent maneuvers.

As part of the Lower Atmospheric Profiling Studies at Elevation- a Remotely-piloted Aircraft Team Experiment (LAPSE-RATE) flight campaign, Islam et al. (2021) created a novel design for the IMet-XQ and IMet-XQ2 housings to meet the aspiration and shielding requirements for the temperature and humidity sensors while avoiding mixed turbulent flow from the propeller wash. The housings function as tubes, drawing air passively by utilizing a pressure differential between the outlet just over the propeller and the inlet beyond the rotor wash. Resulting temperature and relative humidity profiles from ascent and descent patterns remained within the sensor uncertainties indicating the successful implementation of the housing. Ascent-descent deviations were related to sensor response times and was problematic for the slower relative humidity sensor. Therefore, appropriate housing resolves many of the IMet-XQ2 instrument’s issues, however sensor response time delays must be corrected and calibrated for representative boundary layer conditions.

MiniOFS

The MiniOFS is a miniaturized instrument (Table 2) manufactured by Sten Löfving (Optical Sensors, Inc.) that measures visibility parameters. The MiniOFS optical sensor is sensitive to backscattered light from hydrometeors and particulates in a zone about 25 cm (0.25 m) ahead of the sensor. Analog voltage and digital data output ambient solar irradiance, extinction coefficient, and visibility. The sensitivity of the ambient solar irradiance measurement depends greatly on the orientation relative to the sun. The extinction coefficient and visibility parameters are related by the relationship $\beta = \frac{3}{Vis}$. The MiniOFS has a maximum visibility threshold of 4000 m; however, extinction coefficient can be used to calculate trends in visibilities greater than 4000 m with reduced accuracy. If the optical receiver becomes oversaturated through sunlight, nearby object reflections, or obstructions to the sensor, the visibility will display 5000 m. To prevent moisture contamination, a membrane ventilator equalizes the ambient pressure with the internal housing while the sensor is heated a few degrees above the ambient temperature.

Table 2. Table indicating the MiniOFS Sensor Specifications. Manufacturer recommendations suggest a 5-to-10-meter safe zone free of obstructions ahead of the optical receiver.

Analog Output	Analog 0-5 Volt
Digital Output	RS 232
Update Time	30 s
Warmup Time	60 s
Operational Temperature Range	-20 °C to +50 °C
Visibility Range	20 m to 4000 m
Wavelength	850 nm
Optical Output Power (IR LED)	~ 3 mW
Housing	Anodized Aluminum

While the MiniOFS is a cost-effective visibility sensor, evaluation of the MiniOFS for research is still in its relative infancy. Successful MiniOFS identification of dense fog compared well with a Vaisala PWD-11 visibility sensor; however differences in sensor design between the MiniOFS (backwards scattering, lightweight) and PWD-11 (forward scattering, heavyweight) results in MiniOFS overestimation at visibilities below 1 km (Michna et al. 2013). Furthermore, light oversaturation and reflection induced numerous sensor malfunctions and needed correction. Acting as a visibility sensor for a miniaturized balloon-borne cloud water sampler, a MiniOFS contributed to a 70 % collection efficiency when using a 500 m threshold (Zinke et al. 2021). A 1000 m threshold was successful in distinguishing dew events from fog events when investigating non-rainfall water (Riedl et al. 2022).

UAS Platform

The project uses a waterproof, icing-resistant, 1620 mm (5.3 ft) diameter UAV (Table 3). The UAV is custom-built and manufactured by Botlink and uses 29” diameter lightweight carbon fiber propellers with integrated water ingress protection that allows for a maximum takeoff weight of 25 kg (55.1 lbs) and a maximum payload allowance of 6 kg (13.2 lbs). Four 30,000 mAh high density lithium-ion batteries enable payload dependent flight times of around half an hour. Eight total batteries allow for two rapid-succession UAV flights and an hour of maximum mission length. A licensed UAV operator conducts all operations and ensures compliance with FAA waiver restrictions.

Table 3: A table listing the Unmanned Aircraft Vehicle (UAV) specifications for supercooled and low visibility missions. The Pixhawk Cube is a module that integrates autopilot functionality into UAV operation. The Radio Control Controller acts as a ground station for data uplink and visualization to the UAV. The Botlink eXtended Range Datalink (XRD) provides constant monitoring during UAV operations using a Fourth Generation Long Term Evolution (4G-LTE) connection and facilitates real-time data upload. The Firehouse strobe lights enable drone visualization during reduced visibilities. Removable landing gear and arms allow for UAV storage.

Diameter	1620 mm
Maximum Takeoff Weight	25 kg
Maximum Takeoff Payload	6 kg
Flight Time Estimates	32.5 min (4 kg Payload)
	28.9 min (6 kg Payload)
Battery Capacity	4 x 30,000 mAh
Autopilot	Pixhawk Cube
Radio Control (RC) Controller	2.4 GHz, 8 km range
Datalink	900 MHz, Botlink XRD LTE
Lighting	6x Firehouse ARC XL Strobes
Landing Gear	Fixed and Removable
Arms	Removable
Propellers	29" Lightweight Carbon Fiber

A Federal Aviation Administration (FAA) waver permitted UAV operations within low-visibility conditions in the Red River Valley, located at Ice Crystal Engineering (ICE) headquarters in Kindred, North Dakota (Figure 2). Operations are constrained to 400 ft above ground level

(AGL) as part of FAA (part 107) regulations. Low-visibility (< 1 km) missions can occur during daytime hours (sunrise to sunset) whereas high-visibility (> 1 km) missions can occur at any hour. Visual line-of-sight rules are enforced with all UAV missions in the designated airspace south of Ice Crystal Engineering (ICE) headquarters (Figure 2).

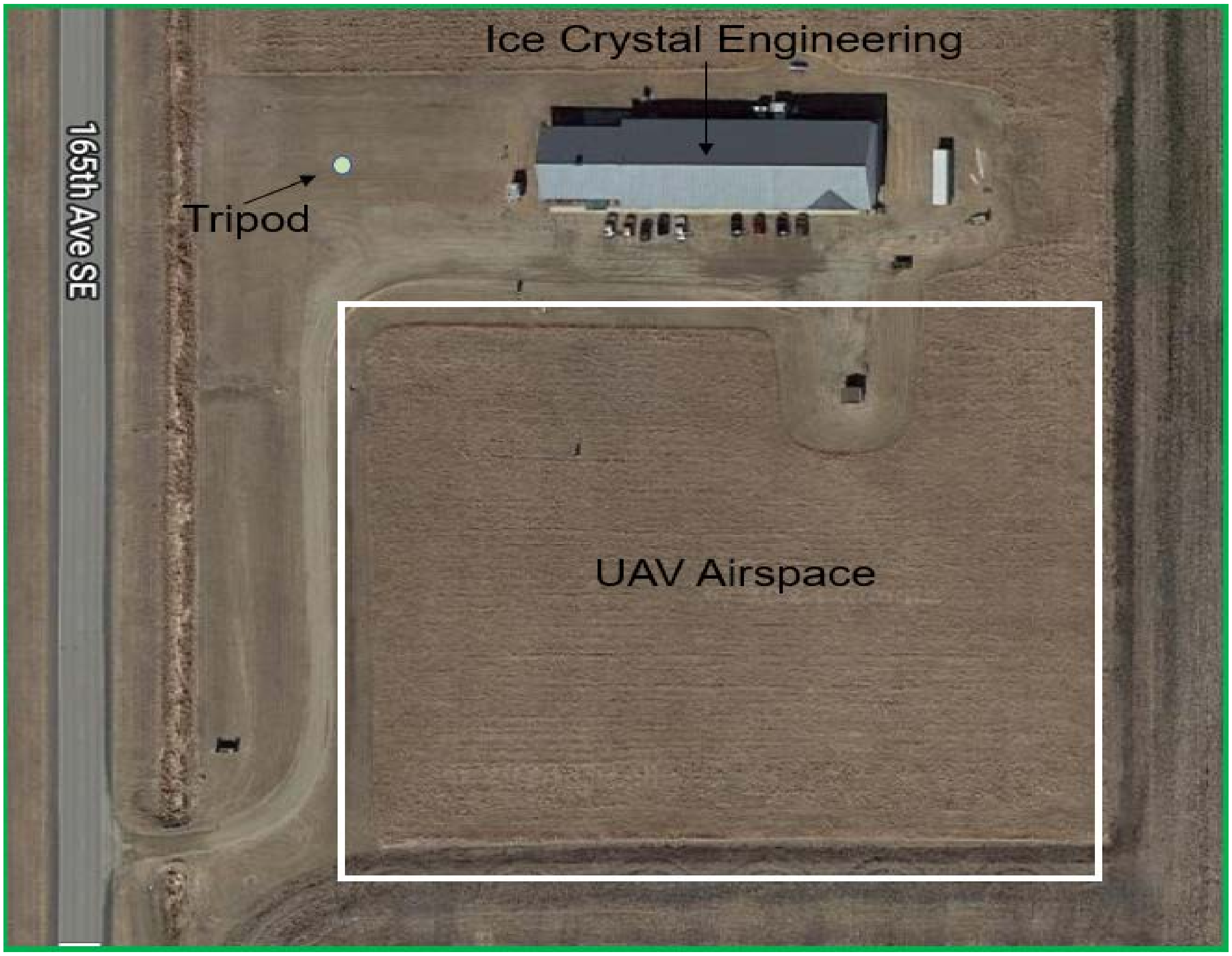

Figure 2. Aerial view of Ice Crystal Engineering (ICE) in Kindred, North Dakota. FAA approved airspace for Unmanned Aircraft Vehicle (UAV) missions is located to the south of building headquarters, with a tripod of instrumentation located to the west of building headquarters.

Based on recommendations by Kimball et al. (2020), both IMet-XQ2 and MiniOFS instruments are attached beneath the main body of the UAV and connected to power and a data acquisition system to create the UAS atmospheric measurements platform (Figure 3). The IMet-XQ2 is displaced around 20 cm (8 inches) ahead of the frame of the UAV and the MiniOFS is displaced around 15 cm (6 inches) to the rear. To avoid direct solar radiation and oversaturation, the MiniOFS is oriented horizontally with the optical receiver facing the ground. Per FAA regulations, any additional components outside of an approved UAV design must remain separate from the UAV electrical system. A 10000 mAh lithium-ion battery powers the Raspberry Pi 4B through an RPI UPSPack Standard V3P expansion board. All sensitive electronics are located within the UAV housing (Figures. 3, 4).

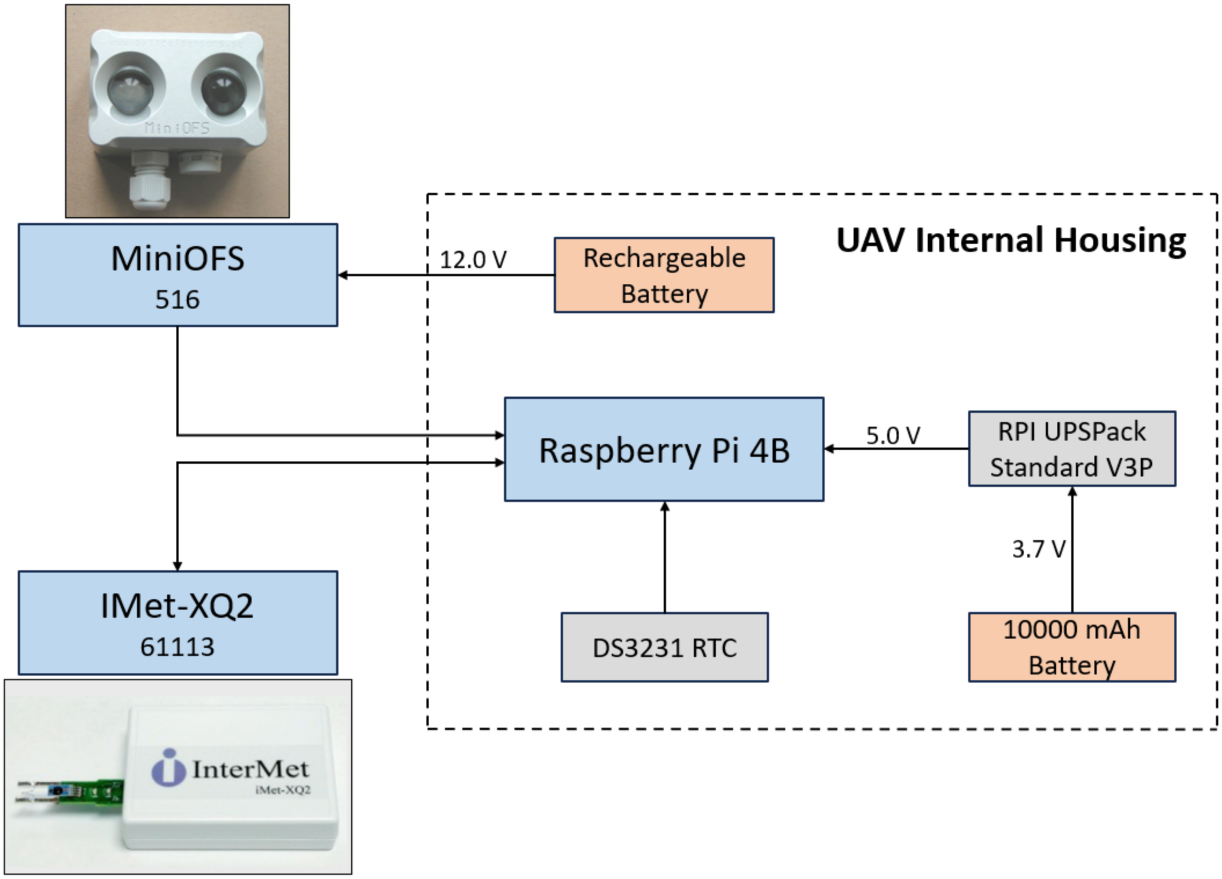

Figure 3. A schematic representing the wiring and components of the Unmanned Aircraft Vehicle (UAV) based, atmospheric measurements system. A Raspberry Pi 4B computer records and stores MinOFS and IMet-XQ2 data through RS-232 serial transmission using a USB converter. A real-time clock module (model DS3231) attached to the Raspberry Pi 4B provides internal time synchronization during UAV missions when the Raspberry Pi 4B is disconnected from an internet source. The 3.7-volt battery supply is transformed to a 5-volt output required for the Raspberry Pi 4B motherboard via the expansion board. Power for the IMet-XQ2 is provided via USB connection to the Raspberry Pi 4B. A separate rechargeable 12-volt battery powers the MiniOFS. Wiring connecting the instruments to the Raspberry Pi 4B within the UAV body utilizes a gap on the underside of the UAV frame.

Figure 4. A picture showing the internal body of the Unmanned Aircraft Vehicle (UAV). The four lithium-ion batteries are displayed in silver, with the internal instrumentation/electrical components placed on top for image visualization. Normally, the internal wiring/electrical components are stored within the gaps of the UAV frame around the lithium-ion batteries.

Ground-based Platform

A ground-based weather station was built to support UAS flight missions, hereby referred as the ‘tripod’ (Figs. 5, 6). For the purposes of redundancy with respect to the UAS platform, IMetXQ2 and MiniOFS instrumentation provide ground-based verification for standard atmospheric and optical conditions. The Raspberry Pi 4B requires a 5-volt power source and powers the IMet-XQ2 and R.M. Young Anemometer through USB connection. The MiniOFS requires a 12-volt power source and is connected separately. Power to the tripod instrumentation platform is facilitated through the nearby ICE building headquarters. All sensitive electronics and wiring are located within the camera box housing. A Raspberry Pi 4B camera module serves as visual confirmation of atmospheric phenomena and is situated towards the front of the housing interior. The MiniOFS is attached to the front exterior of the camera box housing with the optical receiver facing the horizon. The camera box housing is oriented to the north to satisfy oversaturation recommendations from the MiniOFS manufacturer. The ‘master’ half of the bridge is located adjacent to a westward-facing window within ICE headquarters. The ‘slave’ half of the bridge is located on the tripod above the camera box housing and is connected to the Raspberry Pi 4B through a wired ethernet connection. Internet availability allows remote access into the Raspberry Pi 4B computer for efficient software monitoring and maintenance.

Figure 5. A picture showing the ground-based tripod system. The IMet-XQ2 is located in black underneath the radiation sensor on the left side. The Young Anemometer is located at the top of the tripod. The MiniOFS is located at the front of the camera box, outside of view. Power to the system is supplied by Ice Crystal Engineering Headquarters through extension cords.

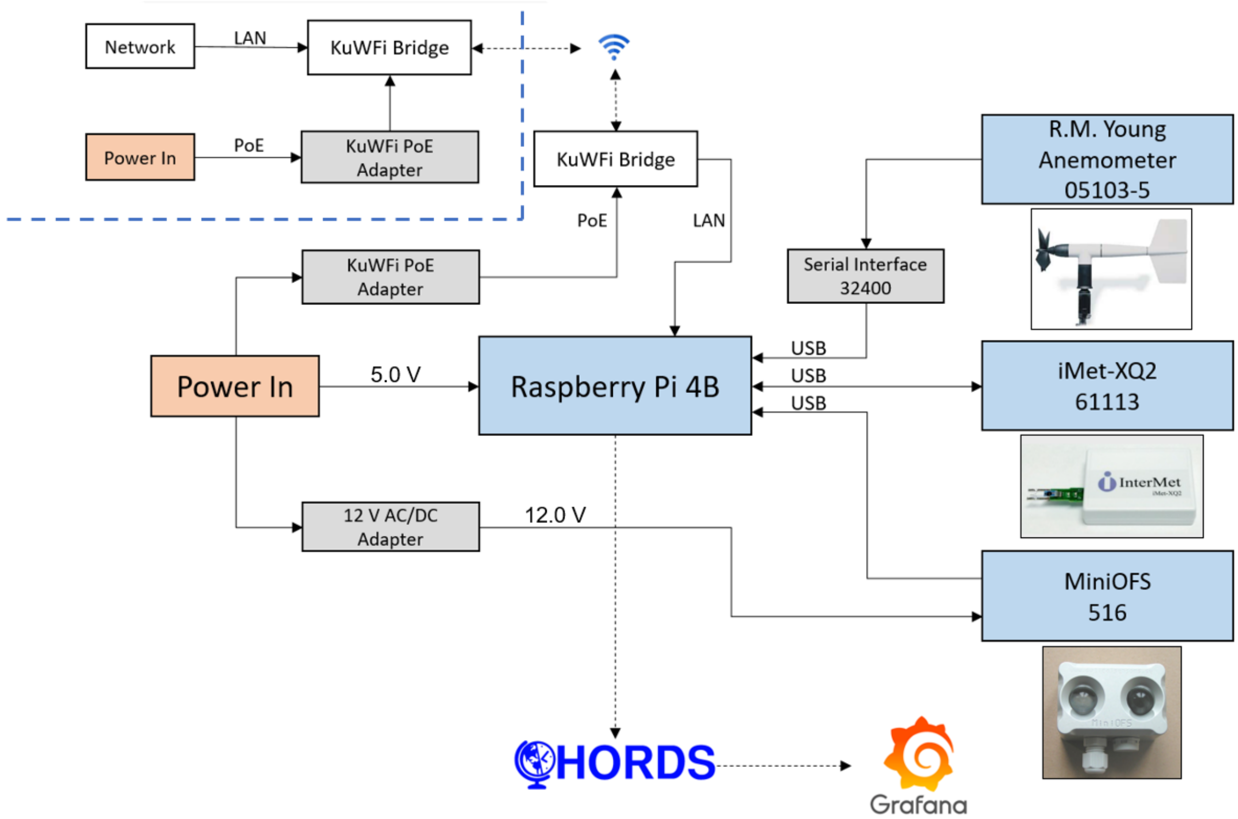

Figure 6. Diagram showing the components of the tripod station. The IMet-XQ2 is situated within a radiation shield to protect the temperature and relative humidity sensors from moisture contamination and direct sunlight. Wind direction and wind speed are measured by an R.M. Young Anemometer (model 05103-5). A Raspberry Pi 4B computer records and stores instrument data. A KuWFi wireless bridge (KuWFi Technology Co., Ltd) provides internet to the Raspberry Pi 4B computer on the tripod The 'master' half of the KuWFi bridge is located near a westward facing window within ICE building headquarters and is designated to the upper-left of the dashed blue line.

Data Acquisition

Data acquisition for all instruments on the UAV and tripod occurs through digital data transmission to a Raspberry Pi 4B. The IMetXQ2 and MiniOFS have direct RS-232 output, whereas analog signal from the R.M. Young Anemometer is converted to digital RS-232 output through a Cambell Scientific serial interface (model 32400). The Airborne Data Processing And Analysis Software Package (ADPAA) is used to extract and process the data on both platforms (Delene 2011). The current version of ADPAA includes python-based instrument acquisition scripts that identify correct port and serial settings (Table 4) and simultaneously record and average data every minute (regardless of sampling rate). For the tripod, averaged data is pushed to a Cloud Hosted Real-Time Data Services (CHORDS) server (https://earthcubeprojects-chords.github.io/chords-docs) through HTPP requests (Figure 6). Data is subsequently visualized through real-time Grafana (https://grafana.com/grafana/dashboards) open-source visualization dashboards. For both platforms, data is stored on local date-designated files on the Raspberry Pi 4B computers.

Table 4: A table showing the serial and sampling rate configurations for the IMet-XQ2, MiniOFS, and R.M. Young Anemometer.

Instrument	Baudrate	Data Bits	Parity	Stop Bit	Sampling Rate
IMet-XQ2	57,600 bits/s	8	No	1	1 s
MiniOFS	1,200 bits/s	8	No	1	30 s
Young	9,600 bits/s	8	No	1	1 s

CHAPTER III: METHODOLOGY

Fog Climatology

The Red River Valley represents a relative minimum in elevation within Manitoba, western Minnesota, eastern North Dakota, and far northeastern South Dakota (Figure 7). In the United States, the Red River Valley comprises the southernmost extent of the Lake Aggasiz basin, an ancient glacial lake formed by the scouring and subsequent melting of the most recent Pleistocene glaciation event (Brooks 2017). The topography of the Red River Valley is therefore defined by its glacial origin; flat and wide expanses of low-elevation terrain surrounded by glacially unaffected higher rolling hills (Figure 8). The atypical shape of the valley, combined with the young relative age of the Red River, creates an ideal location for seasonal flooding (Burn and Goel 2001), wintertime blizzards (Kennedy et al. 2019), and fog potential (Haase 2007).

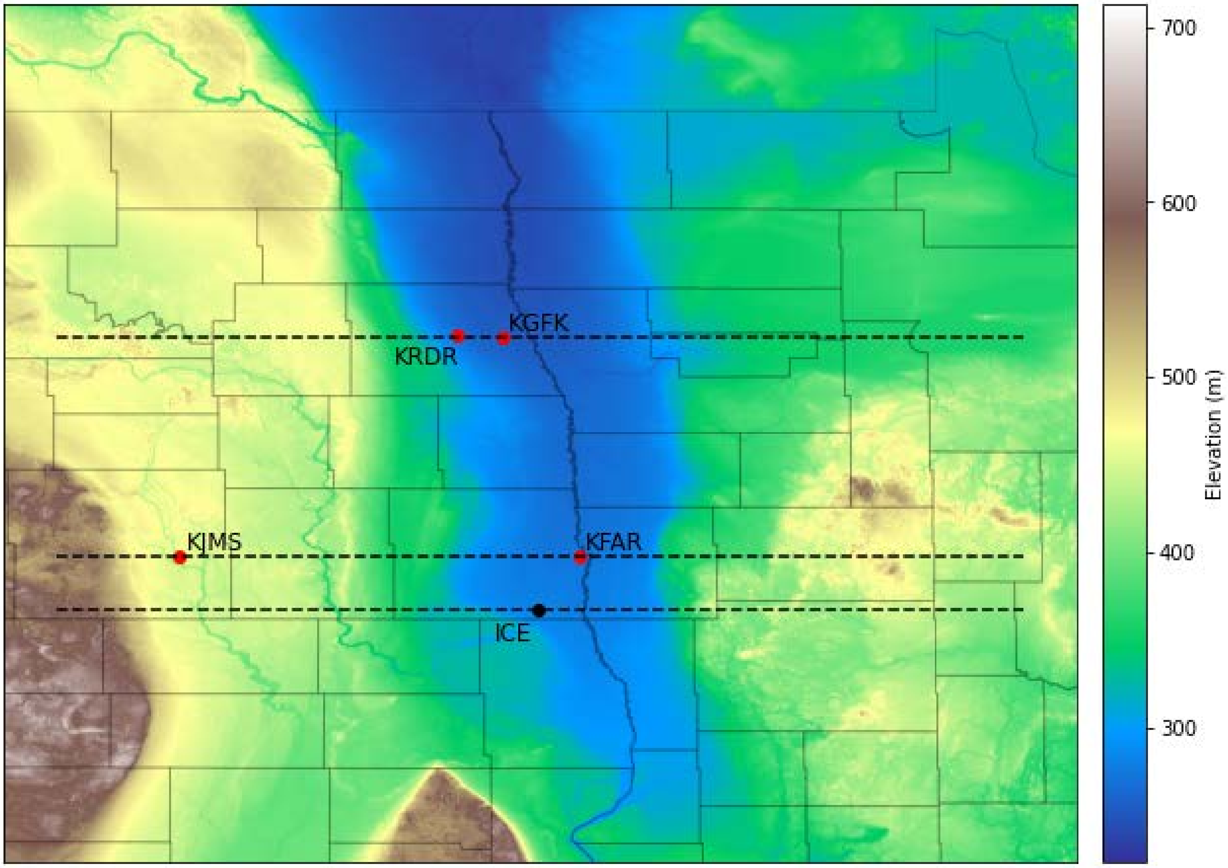

Figure 7. A topographic map showing the Red River Valley of eastern North Dakota and western Minnesota. Locations designated by a red dot are sites used for a 30-year climatological analysis and include Grand Forks International Airport (KGFK), Grand Forks Air Force Base (KRDR), Hector International Airport (KFAR), and Jamestown Regional Airport (KJMS). The location designated by a black dot represents Ice Crystal Engineering headquarters (ICE). The three east-west oriented, black-dotted lines represent cross-sections visualized in Figure 8. Topographic data is provided by the United States Geologic Survey.

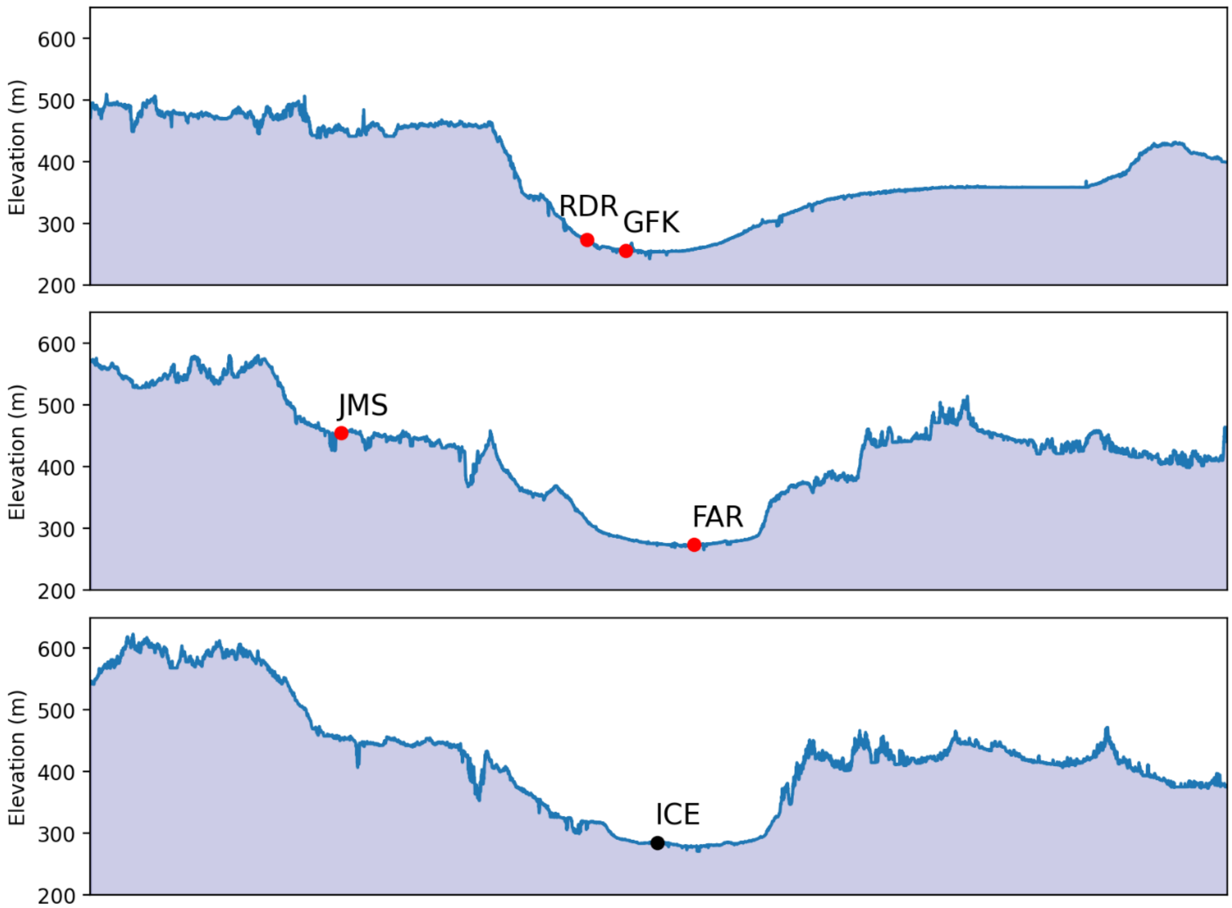

Figure 8. Three east-west topographic cross-sections located at the dotted lines in Figure 7. The cross-section latitudes (top to bottom) are centered at Grand Forks International Airport (GFK) 47.9429°N, Hector International Airport (FAR) 46.9218°N, and Jamestown Regional Airport (JMS) 46.6784°N. The latitudes of RDR and JMS, while not identical to those of GFK and FAR respectively, are close approximations..

While the diurnal bias towards morning fog formation is well understood, literature and data on seasonal fog climatology in the Red River Valley is limited. To that end, fog climatologies are produced from Red River Valley automated surface observing system (ASOS) stations using a 30-year period from 1989-2019. The geographical locations of these stations, with respect to the Red River Valley, are presented in Figure 8. Standard atmospheric parameters are recorded on an hourly basis, with specific research emphasis on temperature, wind speed, visibility, and present weather. The ASOS forward scattering visibility algorithm computes a 10-minute rounded harmonic mean every minute using the equation,

$$\bar{V} = \frac{n}{\frac{1}{V_1} + \frac{1}{V_2} + \cdots + \frac{1}{V_n}}, \qquad 3$$

where $\bar{V}$ is the harmonic mean, $n = 10$, and V_1, V_2, V_n are the 1-minute visibility reports. The newest visibility report is checked against the previous visibility reports, and if it passes a specified threshold, a special observation report is issued outside of the normal hourly reports.

The four ASOS-automated obstructions are fog (FG), mist (BR), freezing fog (FZFG), and haze (HZ). Other obstructions are manually reported by the observer. An obscuration algorithm infers the type of obstruction from concurrent measurements of visibility, temperature, dew point, and present weather. Once the 10-minute harmonic mean visibility drops below 7 statute miles, the algorithm looks at the dew point depression to distinguish between FG, BR, and HZ. When the dew point depression is less than 4 °F (~ 2 °C), FG or BR is reported. When the concurrent visibility is between 11.2 km and 1 km, BR is reported. When the visibility is less than 5/8 statute miles, FG is reported. If the temperature is at or below freezing at the time of an FG report, FZFG is reported. HZ is only reported when the dew point depression is greater than 4 °F (~ 2 °C) and the present weather sensor is not reporting any precipitation.

Instances of fog and/or mist are grouped by hour within each specific calendar day. Instances with concurrent hydrometeor (rain, snow, thunderstorm, drizzle, etc.) or non-hydrometeor (haze, smoke, etc.) conditions are excluded. Special observation reports are common with occurrences of low visibility by ASOS stations; therefore, only the first fog occurrence within each hour is recorded. Wind thresholds (< 10 m/s) are applied to filter out blowing snow events that can mimic fog conditions. Data is additionally subset by temperature (< 0 °C) for supercooled fog climatologies.

Instrumentation Analysis

With newly developed instruments, such as the IMet-XQ2 and MiniOFS, it is important to compare measurements to industry-standard instruments. Hence, in the fall and early winter of 2021, both the IMet-XQ2 and MiniOFS sensors were attached to a University of North Dakota Meteorological Trailer (MetTrailer, http://mettrailer.atmos.und.edu). The MetTrailer was stationed at the Fargo Jet Center, located on the north side of Hector International Airport (KFAR). The Vaisala WXT536 multi-parameter weather sensor (temperature, humidity, pressure, rainfall, wind) and the Campbell Scientific CS125 present weather sensor (temperature, humidity, visibility) are used as instrument comparisons to the IMet-XQ2 and MiniOFS. Data from all instruments are recorded every minute from September 16th, 2021 to December 2nd, 2021.

UAS Missions

An operational framework implementing the UAS platform during a theoretical supercooled fog abatement project centers on a couple objectives:

1. Demonstrate a successful collection of in-situ atmospheric data within the fog layer and determine the top of the fog.
2. Implement UAS flight patterns (racetrack, box, etc.) to release an appropriate amount of seeding material near fog top.
3. Maintain UAS operations until changing conditions indicate suitable fog clearing has been done or UAS operational constraints dictate cessation of operations.

Hence, flight patterns for UAS research are related to fog seeding operations. Similar to efforts by Chong et al. (2020) and Islam et al. (2021), vertical profiles to 400 ft AGL are attempted in both high and low visibility conditions. In-situ profiling of temperature, humidity, and visibility aims to resolve fog characteristics and determine an approximate height of the cloud layer. Hovering maneuvers demonstrate in-situ monitoring of conditions for verification and instrument calibration purposes. Racetrack and box flight patterns simulate UAV maneuvers that would be accomplished during dispersal operations. Finally, mission longevity analysis during high and low visibility conditions helps establish temporal limits on UAS platform performance.

CHAPTER IV: RESULTS

Fog climatologies are visualized through heatmaps that utilize a percentage chance of hourly occurrence. This probability of occurrence is defined as follows,

$$P_h = \left(\frac{n_h}{N}\right) \times 100, \qquad 4$$

where P_h is the percentage probability of hourly occurrence, n_h is the number of occurrences during the hourly period, and N is the total possible outcomes in the sample space. For the 1989-2019 sample period, N is 30 since there is one possible occurrence per year.

Seasonally, P_h increases during the winter and early spring months and decreases sharply by April (Figure 9). The early morning hours are most favored for higher P_h, decreasing dramatically beyond sunrise. The beginning of July displays the earliest hourly period for maximum P_h (4 – 5 CST), with late December into early January as the latest (8 – 9 CST). Where these higher trends of P_h intersect during the early morning hours of March, P_h peaks close to 37 percent. Similar trends in temporal extent and magnitude of P_h are seen at KGFK, KFAR, and KJMS as at KGFK (Figure 9). KRDR lags in magnitude compared to the other stations. KJMS and KRDR (and to a lesser extent KGFK and KFAR) exhibit temporally banded features of higher relative P_h during March. All stations report a lull of P_h during late September into the first half of October for all hourly periods.

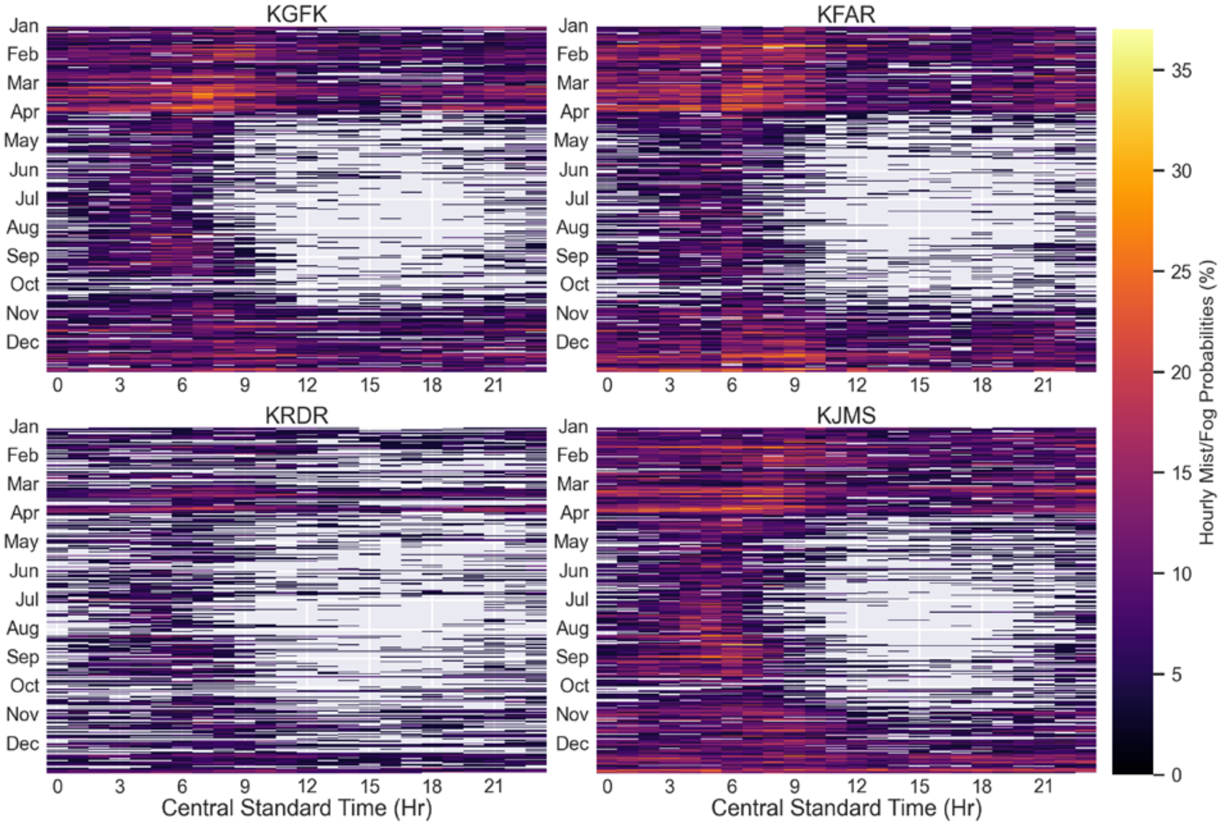

Figure 9. Hourly probability heatmap plots showing the amount of mist and/or fog at Grand International Airport (KGFK), Hector International Airport (KFAR), Grand Forks Air Force Base (KRDR), and Jamestown Regional Airport (KJMS) from 1989-2019.

Implementing a 10 meters per second wind threshold (Figure 10), while the trend of higher P_h in the early morning hours remains, the winter and early spring bias in P_h is drastically reduced. Both the temporal extent and magnitude of P_h are decreased throughout all hourly periods. The groups of higher P_h are also less temporally consistent. Periods of high P_h are immediately adjacent to periods of low or zero P_h (no mist/fog occurrences) resulting in a “noisier” heatmap. When comparing all North Dakota locations, there is good consensus with the observed trends at KGFK (Figure 10). Outside of subtle hints at KRDR and KJMS, the temporal bands of higher P_h during March have largely disappeared. While still lessened, the P_h magnitudes at KRDR are closer to the rest of the stations. Two early morning regions of locally higher P_h are evident: a mid-July to mid-September peak, and mid-February to late March peak. KJMS most strongly emphasizes the local maxima in P_h (20 %) during July and August.

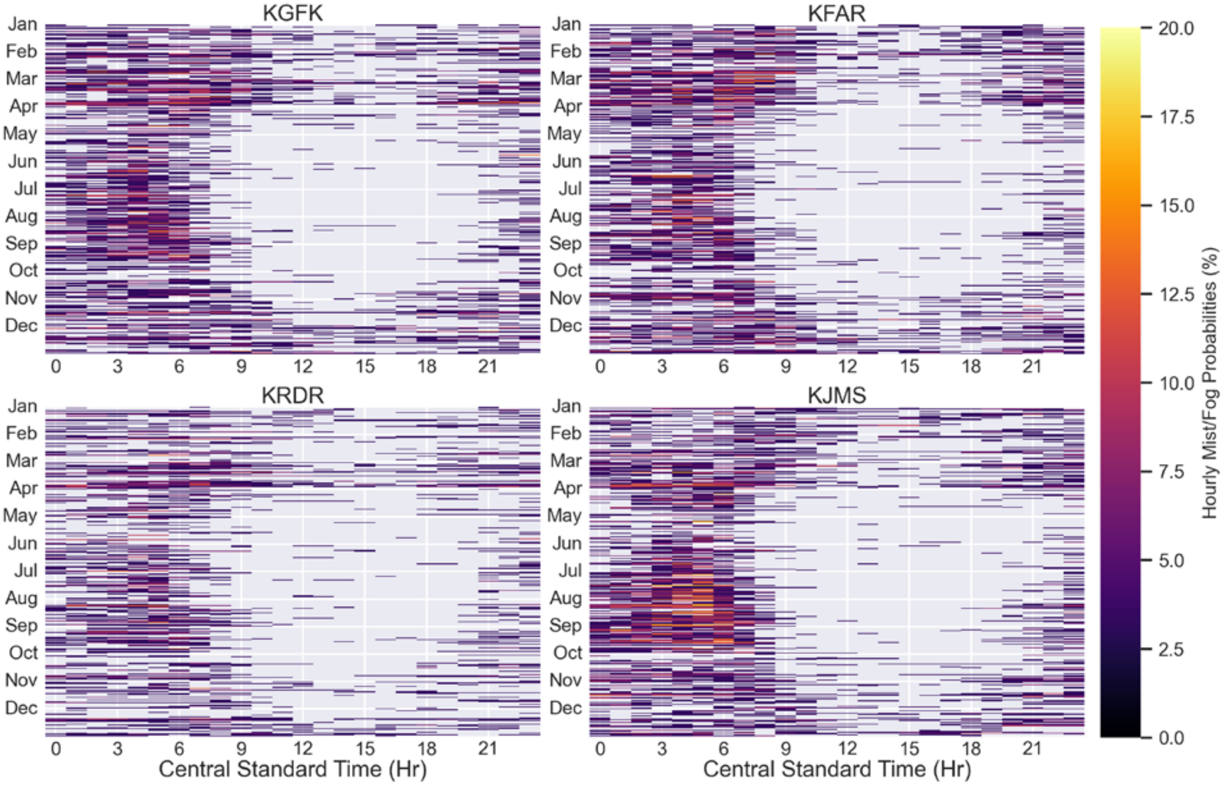

Figure 10. Heatmap plots using the same format as Figure 9 but filtered to remove wind speeds above 10 m/s.

In addition to a wind speed filter, Figure 11 applies a temperature (< 0 °C) filter to hourly mist/fog probabilities at KGFK to obtain super-cooled fog occurrences. Fog occurrences during the summer months are no long present; however, the early morning occurrence of higher P_h remains but is considerably less prominent. A group of locally elevated P_h is centered during the morning hours of February and March. These observed trends at KGFK occur in all stations (Figure 11) with the group of maxima most prevalent at KFAR (17 %).

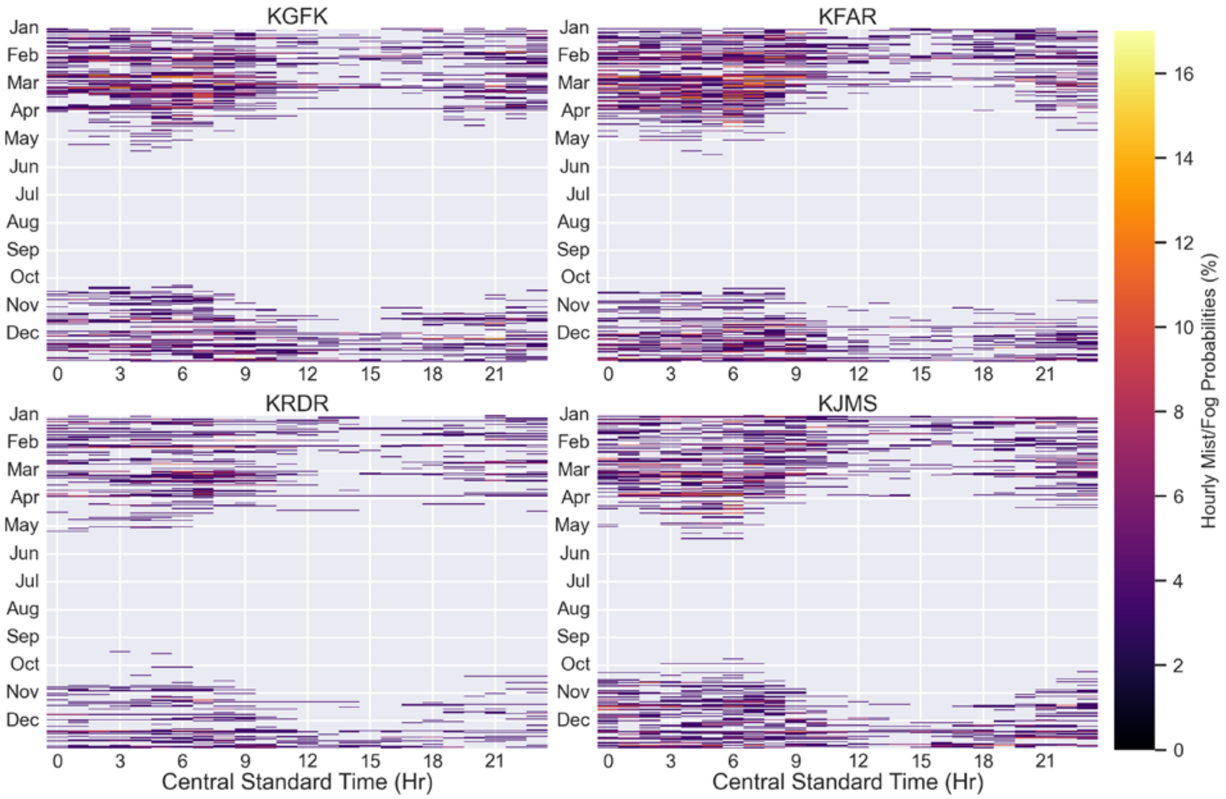

Figure 11. Heatmap plots using the same format as Figure 10, but with temperatures below 0 °C.

Instrumentation comparisons are implemented using least squares, linear regression analysis. Taking a collection of data points (x,y), there is a line that can be fitted using the linear equation,

$$\hat{y} = \hat{\beta}_1 x + \hat{\beta}_0, \qquad 5$$

that best fits the data wherein minimizing the sum of the squared errors with respect to the line. The coefficients $\hat{\beta}_1$ and $\hat{\beta}_0$ are defined as follows:

$$\hat{\beta}_1 = \frac{SS_{xy}}{SS_{xx}}, \qquad 6$$

$$\hat{\beta}_0 = \bar{y} - \hat{\beta}_1 \bar{x}, \qquad 7$$

where,

$$SS_{xx} = \sum x^2 - \frac{1}{n}\left(\sum x\right)^2, \qquad 8$$

$$SS_{xy} = \sum xy - \frac{1}{n}\left(\sum x\right)\left(\sum y\right), \qquad 9$$

$\bar{x}$ is the mean of the x-values, $\bar{y}$ is the mean of the y-values, and n is the total number of data points. The WXT536 and CS125 instruments are used as independent (or predictor) x-values and the IMet-XQ2 and MiniOFS instruments, respectfully, are the dependent (or response) y-values. The coefficient of determination (r^2) is represented as the proportion of variation in the dependent y-values that can be explained by a simple linear regression model. r^2 is defined as follows:

$$r^2 = 1 - \frac{SSE}{SST}, \qquad 10$$

where SSE and SST are the error sum of squares and total sum of squares respectively:

$$SSE = \sum (y_i - \hat{y}_i)^2 = \sum \left[y_i - \left(\hat{\beta}_0 + \hat{\beta}_1 x_i\right)\right]^2, \qquad 11$$

$$SST = \sum (y_i - \bar{y})^2 = \sum {y_i}^2 - \frac{(\sum y_i)^2}{n}. \qquad 12$$

$r^2 = 1$ indicates a perfect linear correlation. The standard error of estimate (SE) is another method for measuring the amount of error in a least squares linear regression and is defined as,

$$SE = \sqrt{\frac{(1 - r^2)\sum(x_i - \bar{x})^2}{(n - 2)\sum(y_i - \bar{y})^2}} \qquad 13$$

$\hat{y}$, r^2, and SE are calculated and residuals are plotted for each linear regression. Due to differing maximum observable visibilities between the MiniOFS (4 km) and CS125 (90 km), regression analysis is performed on a filtered data set for visibility below 4 km. Based on MiniOFS overestimation concerns (Michna et al. 2013), regression analysis is also performed on a filtered data set for visibility below 1 km.

Linear regressions comparing the IMet-XQ2 temperature sensor to both the CS125 and WXT536 temperature sensors show strong correlation (Figure 12). r^2-values for both sensors are

0.999 with considerably low values for SE. Values for $\hat{\beta}_1 \approx 1$ and $\hat{\beta}_0 \approx 0$ approach a one-to-one linear relationship for IMet-XQ2 temperature sensor comparisons to the CS125 and WXT536 temperature sensors. Scatter plots show tight clustering around $\hat{y}$ with all residuals less than $|4.5|$ and the majority less than $|1.0|$. For both comparisons, there seems to be greater clustering of positive residual outliers and particularly between 2.5 °C and 7.5 °C. The IMet-XQ2 relative humidity linear regression comparisons to the CS125 and the WXT536 also show a strong linear correlation; $r^2 = 0.978,\ 0.975$ respectively (Figure 13). However, discrepancies arise as $\hat{\beta}_1$ (slope) values of 0.9096 and 0.8356 show a departure from one-to-one relationships. Residual magnitudes increase with higher relative humidities and is reflected in a greater spread of data at relative humidity values less than 40 percent. SE values are an order of magnitude higher (10^{-4}) with the relative humidity linear regressions than compared to the temperature linear regressions (10^{-5}).

Due to the discrepancies of maximum observable visibilities between the MiniOFS (4 km) and CS125 (80 km) visibility sensors, Figure 14 shows the linear regression for the MiniOFS and CS125 visibility sensors when both instruments are recording visibilities below or equal to 4 kilometers. An r^2 value of 0.654 and an SE magnitude of 10^{-2} indicate weaker linear correlation between the two sensors. There is considerable spread in the data and residuals, albeit a tighter spread within visibilities less than 2000 meters. Clustered bands of data are evident in the regression plot and emphasized in the residuals. However, no fog events were captured during this sampling window. Figure 15 displays a linear regression for the MiniOFS and CS125 visibility sensors during a fog event at the MetTrailer on March 22nd, 2022. Better linear correlation occurs as indicated by an increased r^2 value of 0.716 for the 1 km regression. A tighter spread in the data and residuals again occurs at the lowest visibilities. A $\hat{\beta}_1$ value of 0.8850 and $\hat{\beta}_0$ value of 111.90

for the 1 kilometer regression indicate an increasing departure from a one-to-one relationship at the lower visibilities and is evident in the clustering trends.

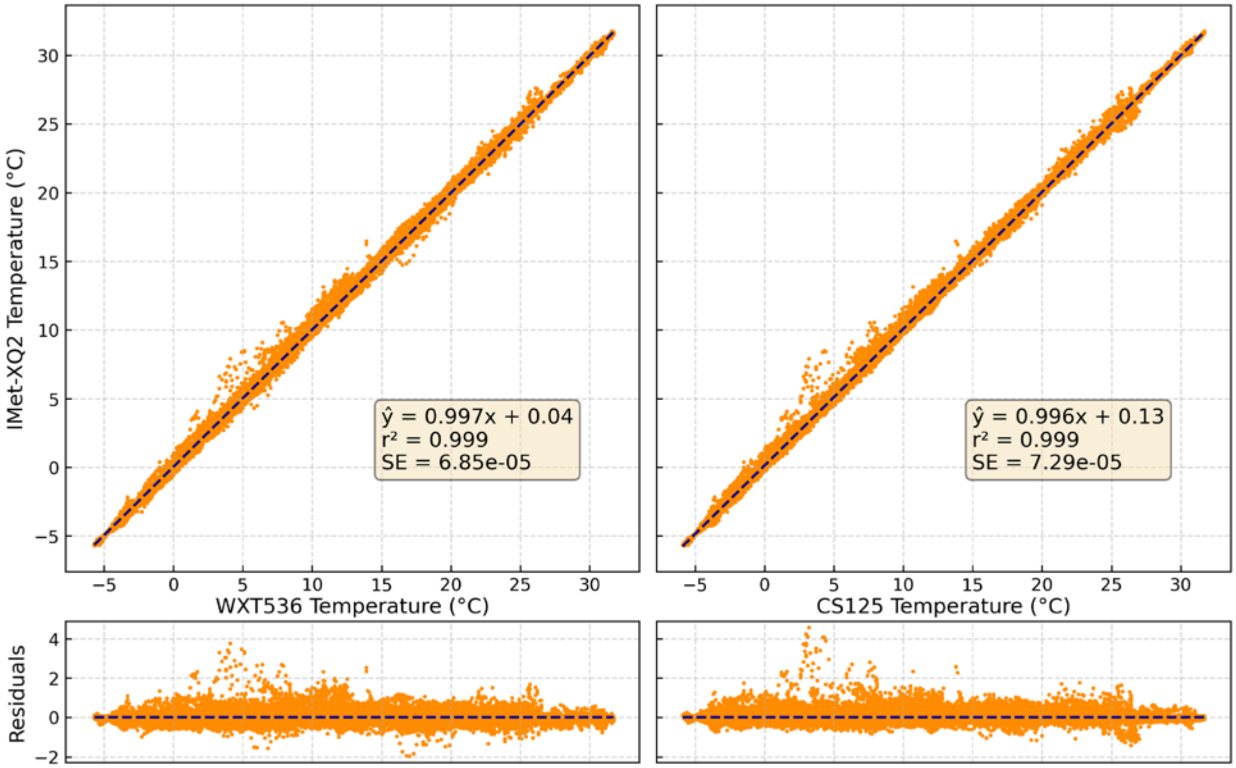

Figure 12. A panel of linear regression plots comparing the IMet-XQ2 Temperature vs. WXT536 (left) and CS125 (right) temperature sensors with secondary plots of residuals. Statistics of the regression are displayed in the bottom left panel of each panel within the respective regression plot. From top to bottom: best-fit regression line ($\hat{y}$), coefficient of determination (r^2), and standard error (SE). Statistics assume a normal distribution of residuals.

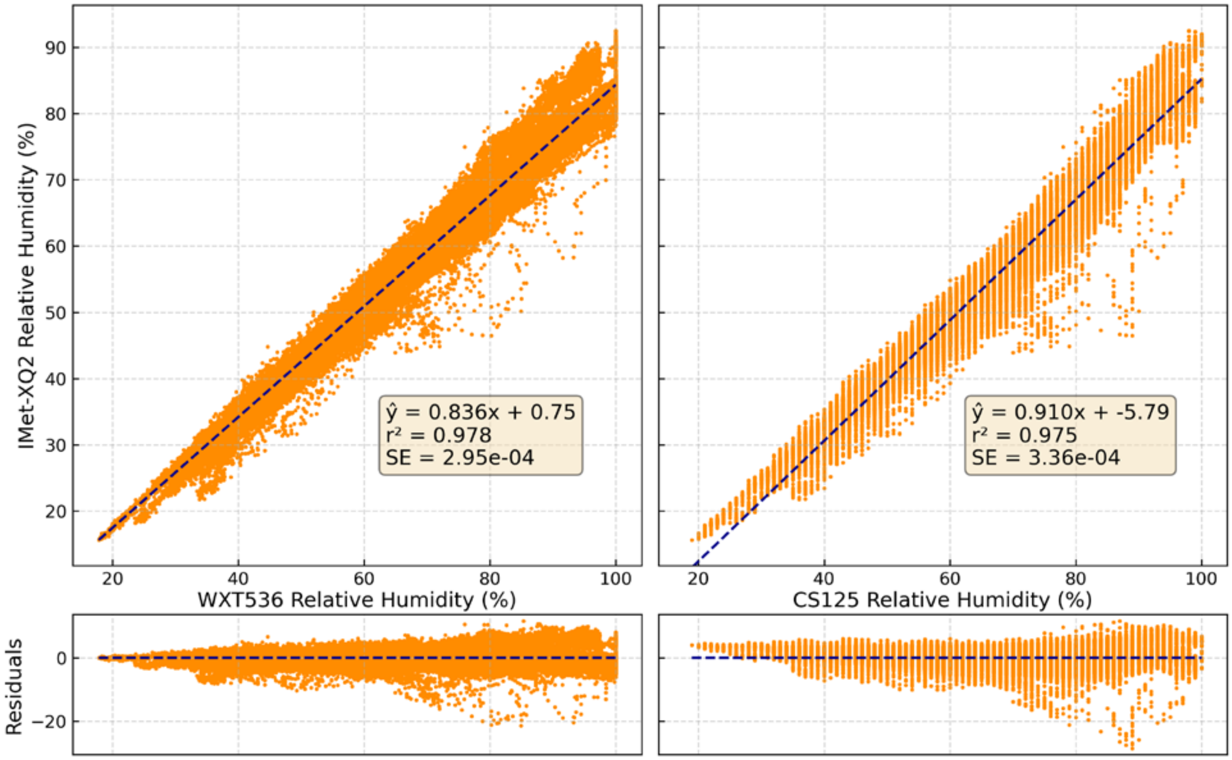

Figure 13. A panel of linear regression plots using the same format as Figure 12, but with a comparison of IMet-XQ2 relative humidity vs. WXT536 (left) and CS125 (right) relative humidity.

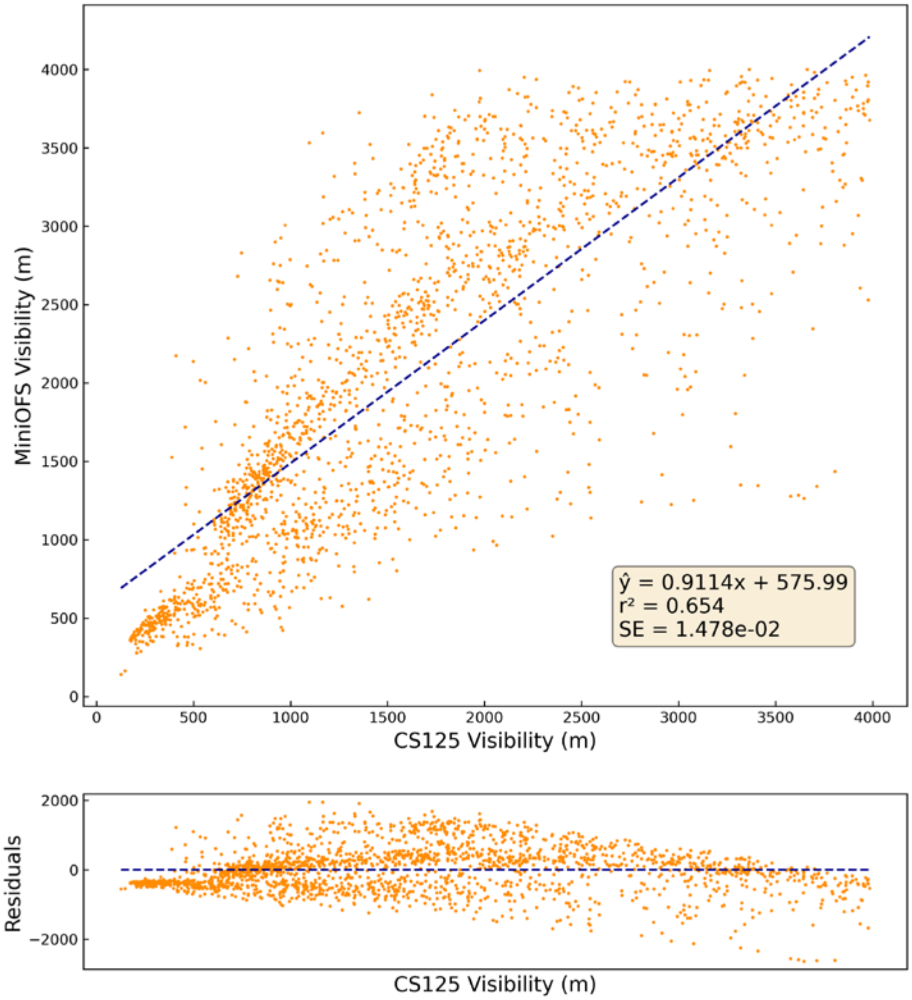

Figure 14: A linear regression plot comparing the MiniOFS and CS125 visibility sensors when recording measurements below 4000 m.

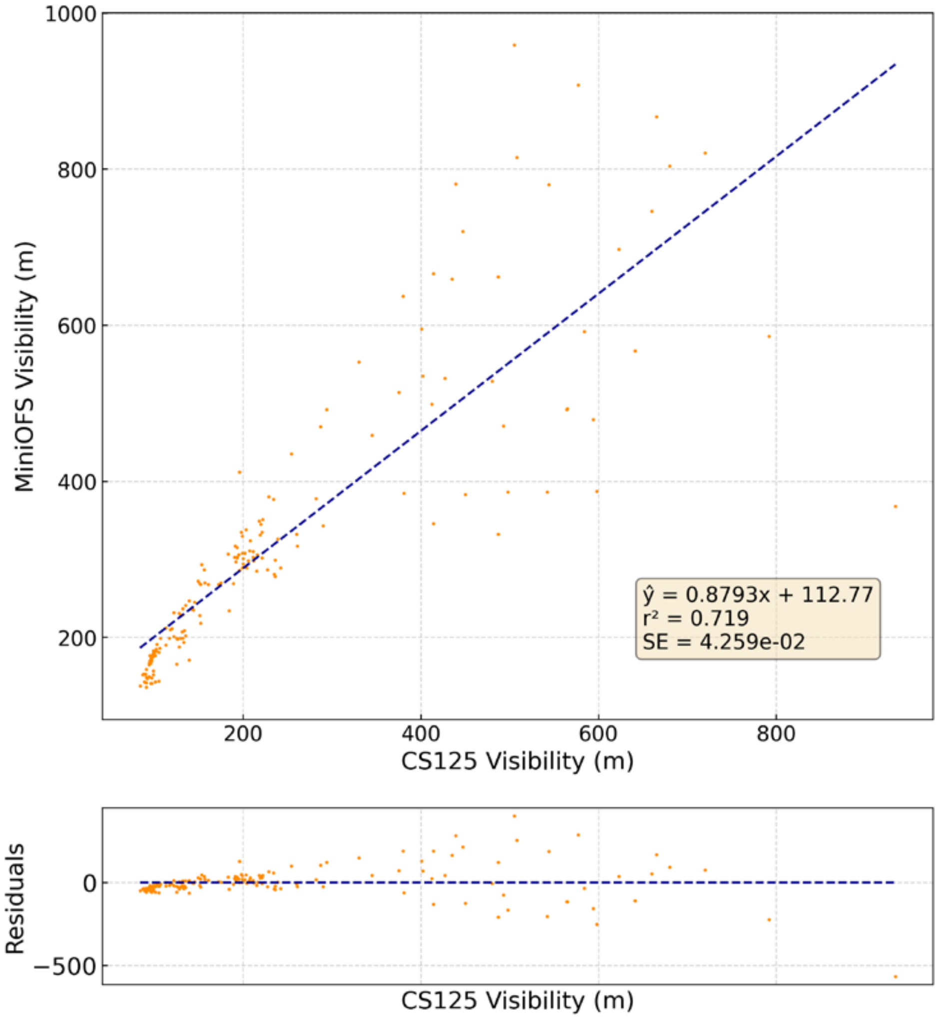

Figure 15. A linear regression plot using the same format as Figure 14, but during a fog event on March 22nd, 2022 when the visibility sensors are recording measurements below 1000 meters.

CHAPTER V: UAS MISSIONS

The usage of the UAS platform in low visibility conditions highlighted the process and prerequisites necessary for efficient and successful implementations. Acquisition of FAA wavers allowing low visibility UAS missions within fogs took over two years of coordinated efforts from Weather Modifiction International and the University of North Dakota beyond the initial project proposal. UAS airspace approval at Ice Crystal Engineering headquarters followed shortly thereafter and proved an essential base for UAS operations. Internet and power accessibility, detachment from major population centers, and a clear unobstructed field of vision allowed for undisturbed line-of-sight visuals during all high and low visibility missions. The licensed UAV pilot safely operated the drone in coordination with the on-station flight scientists with no major accidents or mechanical failures.

Forecasting occurred over several days prior to a potential fog event. Once a period was designated favorable for development, communication between the UAV pilot and flight scientists designated an ideal mission start time. Due to low-visibility FAA-regulations on UAS operation, start times usually occurred shortly after sunrise. Conditions were monitored throughout the morning of potential operations via satellite and regional ASOS observations. If conditions were deemed acceptable or low visibilities were reported regionally, the UAV mission commenced as planned. Procedures for proper functionality of the UAV and attached instrumentation were performed before every flight mission. Over the course of March 2023, eight successful UAV flights occurred over five days. Two of the days occurred in clear-air conditions and three in low-visibility/foggy conditions. In total, fourteen vertical profiles (Table 5), fifteen hovering maneuvers, two racetrack patterns, and one box pattern were successfully executed.

Table 5: Vertical profiles performed during the March 2023 UAV flights. Times reported are in central standard time.

Date	Visibility Conditions	Vertical Profiles	Ascent Start	Ascent End	Descent Start	Descent End	Instrument Status
3/7/2023	No Fog	1	17:59:48	18:00:58	18:01:12	18:02:54	Both
3/13/2023	No Fog	2	15:14:26	15:18:03	15:18:21	15:22:42	Both
			15:22:50	15:26:36	15:27:00	15:32:07	
3/15/2023	Fog	4	08:07:28	08:10:12	08:10:27	08:15:15	MiniOFS only
			08:16:29	08:18:16	08:18:39	08:23:46	
			08:46:32	08:49:28	08:50:35	08:53:43	
			08:53:49	08:55:05	08:55:06	08:56:37	
3/23/2023	Fog	4	08:19:56	08:22:48	08:23:10	08:26:17	MiniOFS only
			08:30:22	08:33:52	08:34:52	08:37:28	
			08:45:30	08:46:52	08:48:39	08:49:54	
			09:16:21	09:21:05	09:22:28	09:27:20	
3/24/2023	Fog	3	08:02:26	08:05:32	08:06:38	08:09:27	Both
			08:14:08	08:22:47	08:23:54	08:25:30	
			08:39:42	08:42:48	08:44:01	08:47:31	

March 7th 2023

Strong surface high pressure and ridging aloft dictated weather conditions on March 7th, 2023. As such, clear skies and high visibilities produced good conditions for the first clear-air test flight of the UAS platform during the afternoon and early evening. Instrumentation on the tripod and UAV platform were operational for the flight mission. Surface temperatures were reported -11 °C by the tripod and just shy of -9.5 °C by the drone instrumentation upon UAV power activation at 17:56:30 CST (Figure 16). Moisture was slowly increasing throughout the day, with relative humidities of both platforms reporting 64 percent upon mission start. UAV power activation occurred at 17:56:30 CST. Initial warmup and calibration procedures occurred for the first two minutes. One ascent-descent vertical profile was successfully implemented from 17:59:48 CST to 18:02:54 CST. The ascent profile started at 100 feet AGL, climbed to a maximum altitude of 400 feet AGL, and descended to 75 feet AGL. The UAV was powered down shortly thereafter at 18:04:01 CST, resulting in a total mission length of 7 minutes and 32 seconds.

The lower atmosphere was largely isothermal during the vertical profile maneuver, as indicated by near constant temperature and dew points of -10 °C and -15.5 °C respectively (Figure 18). Above 250-meters AGL, temperatures rapidly fluctuated between -9 °C and -10 °C while relative humidities (with respect to water) dropped below 60 percent. Both the ascent and descent profiles are in good agreement. A downward shift in the descent profile relative to the ascent is noticeable in both the temperature and relative humidity measurements. Visibilities throughout the vertical profiling reported the maximum 4000 meters, further indication of clear-air conditions.

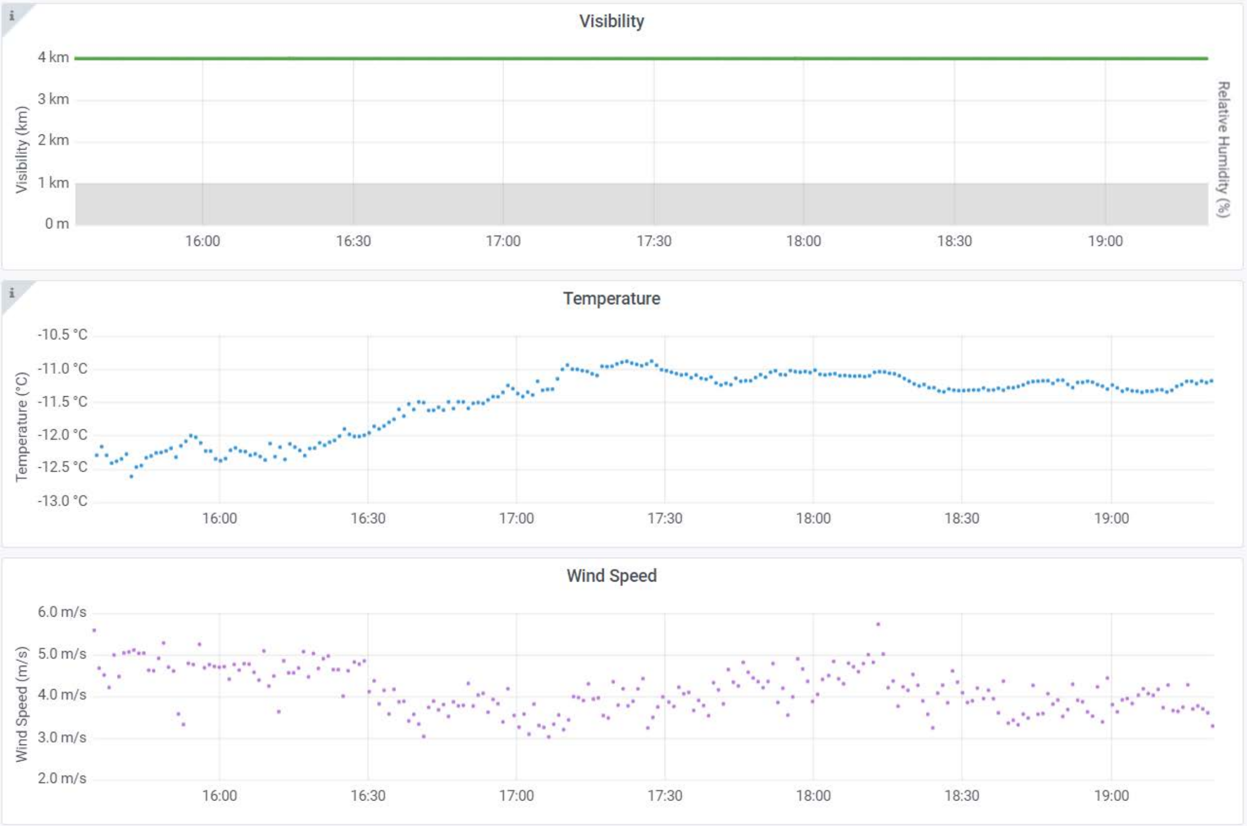

Figure 16. A panel of tripod visibility (green), temperature (blue), and wind speed (purple) time series plots recorded by the IMet-XQ2 on March 7th, 2023. Data is visualized through the Grafana open-source software dashboards. The gray shaded area in the visibility plot represents the 1 km threshold for visibility reductions designated as fog. All times are reported in central standard time (CST). The March 7th UAV mission occurred between 17:56 CST and 18:04 CST.

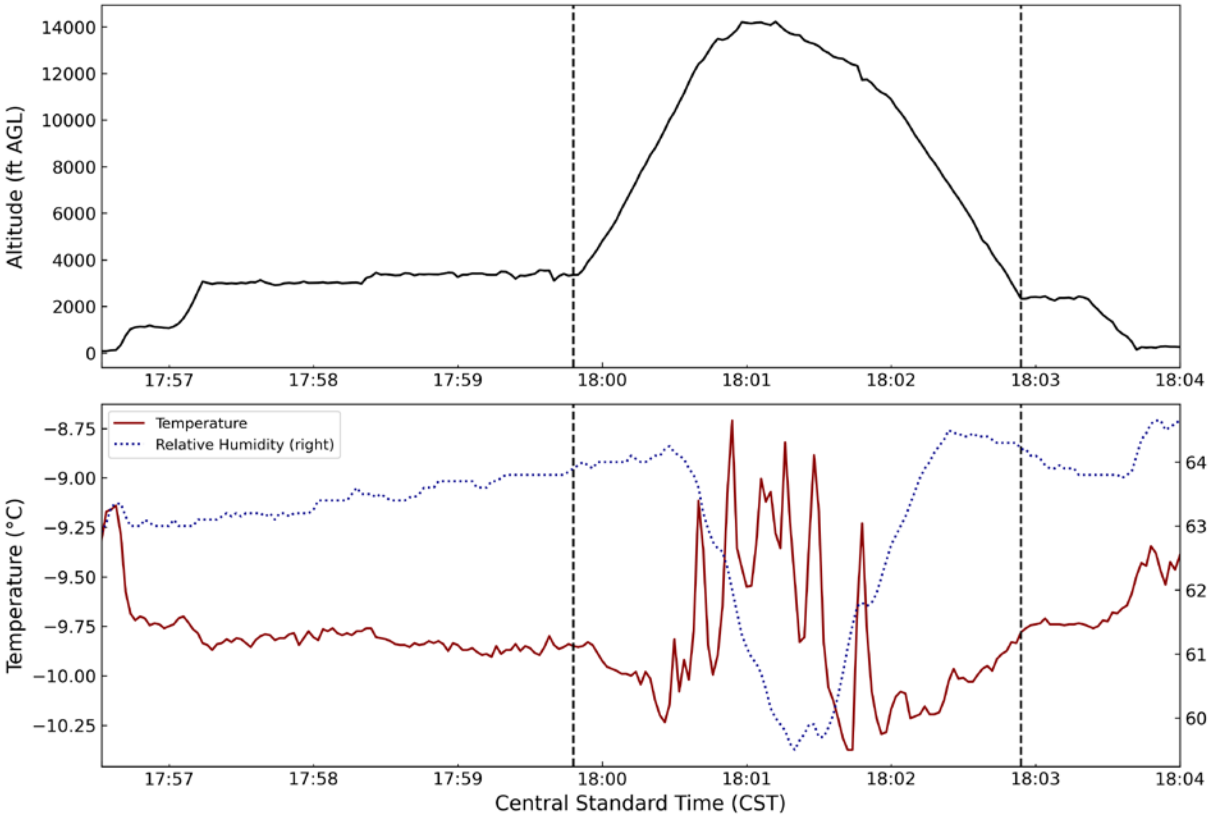

Figure 17. A panel of plots representing UAV altitude (black), temperature (red), and relative humidity (blue dotted) measurements during the March 7th, 2023 flight mission. Vertical black dashed lines indicate the start (17:59:48 CST) and end (18:02:54 CST) times for the vertical profile maneuver.

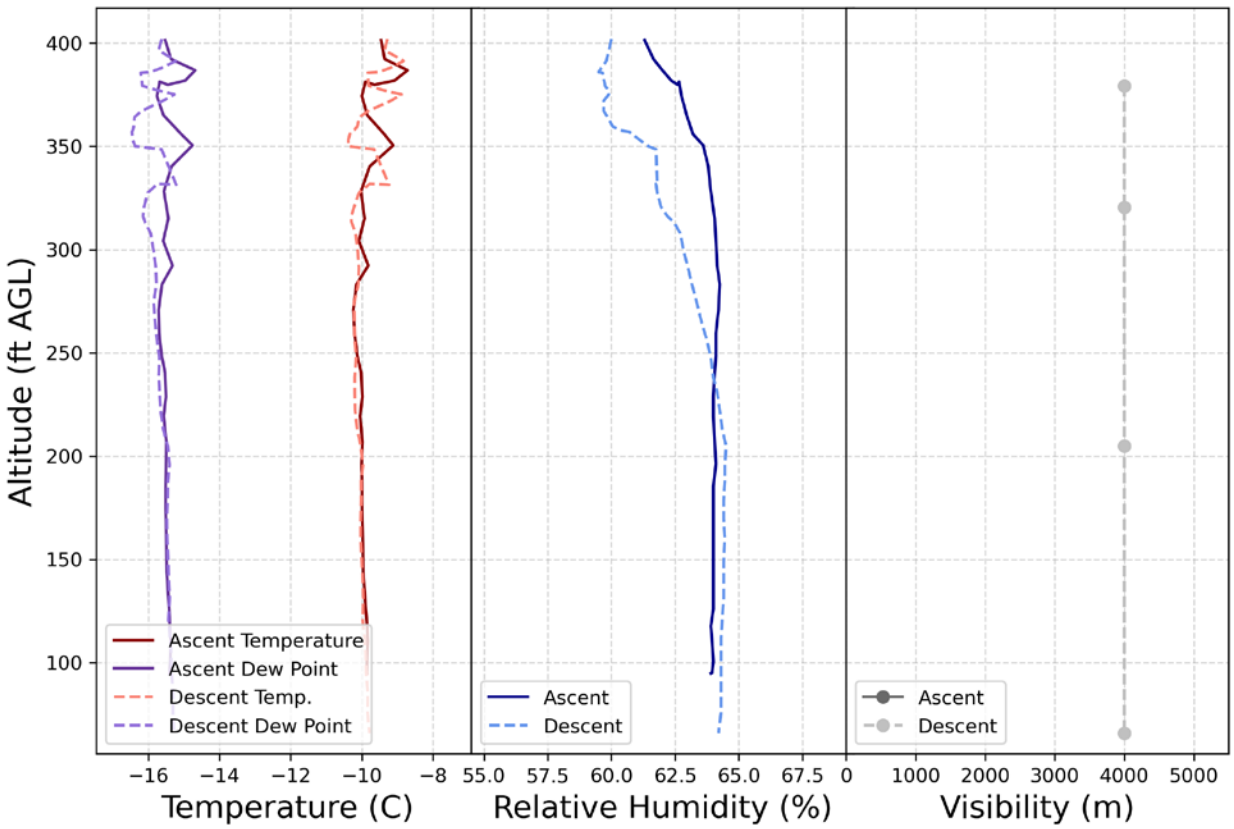

Figure 18. A panel of plots representing temperature (red), dew point (purple), relative humidity (blue), and visibility (gray) during the March 7th, 2023 vertical profiling maneuver between 17:59:48 CST and 18:02:54 CST. The ascent profiling is represented as solid colors and the descent profiling represented as dashed colors.

March 13th 2023

A strong surface high pressure stretched from southern Manitoba into the northern Great Plains through the day on March 13th, 2023. Ridging and subsidence aloft induced clear skies and calm surface conditions for a second UAV clear-air test flight. All instrumentation on both platforms was functional at the time of the afternoon mission. UAV power activation occurred at 15:12:47 CST. Two vertical profiling maneuvers occurred between 15:14:26 CST and 15:32:07 CST, immediately followed by an extended hovering period ending at 15:44:45 CST (Figure 19). Two racetrack maneuvers at 15:48:26 CST – 15:52:18 CST and 15:54:08 CST – 15:55:35 CST were also conducted. The UAV was powered down at 15:57:38 CST, resulting in a total mission length of 44 minutes and 51 seconds.

Winds at the surface were reported light and variable by the tripod; speeds never increasing above 1.6 meters per second for the duration of the mission (Figure 20). At mission start, tripod temperatures ranged between -9 °C and -9.5 °C, with 20 ft AGL UAV temperatures settling to -9.5 °C just before the vertical profiling maneuvers (Figure 21). Surface temperatures spiked to -4 °C after 15:30 CST, fluctuating substantially to a maximum of -2.48 °C by 16:16 CST. Both vertical profiling maneuvers displayed an isothermal atmosphere up to 400 feet AGL with near constant temperatures of -10 °C throughout the atmospheric column (Figs 22, 23). Relative humidity measurements during the first profiling maneuver varied considerably between the ascent (43 - 44 percent) and descent (55 percent) below 250 ft AGL, resulting in considerable dew point differences between the ascent (-20 °C) and descent (-17.5 °C). Above 300 ft AGL, relative humidity measurements had closer agreement. The second profiling maneuver had better correlation for relative humidity measurements between the ascent and descent. Visibility measurements for both profiling maneuvers recorded 4000 m, with lowered visibilities towards the surface related to sensor obstruction issues with the ground.

The hovering maneuver occurred between 15:34:04 CST and 15:43:16 CST at a constant 7.5 feet AGL of altitude (Figure 24). Outside of a singular instance of movement indicated by the latitude change around 15:38 UTC, the maneuver was successful. Temperatures fluctuated between -8.5 °C and -9.0 °C, with relative humidities between 43 percent and 50 percent. The first racetrack pattern consisted of four alternating horizontal maneuvers as shown on (Figure 25). The temperature measurements mimicked this pattern, alternating cyclically between -9.0 °C and -8.2 °C. The relative humidity varied between 46.5 percent and 48.5 percent and responded more subtly to the maneuvers. A second racetrack pattern utilizing two alternating horizontal maneuvers displayed similar results to the first (Figure 26).

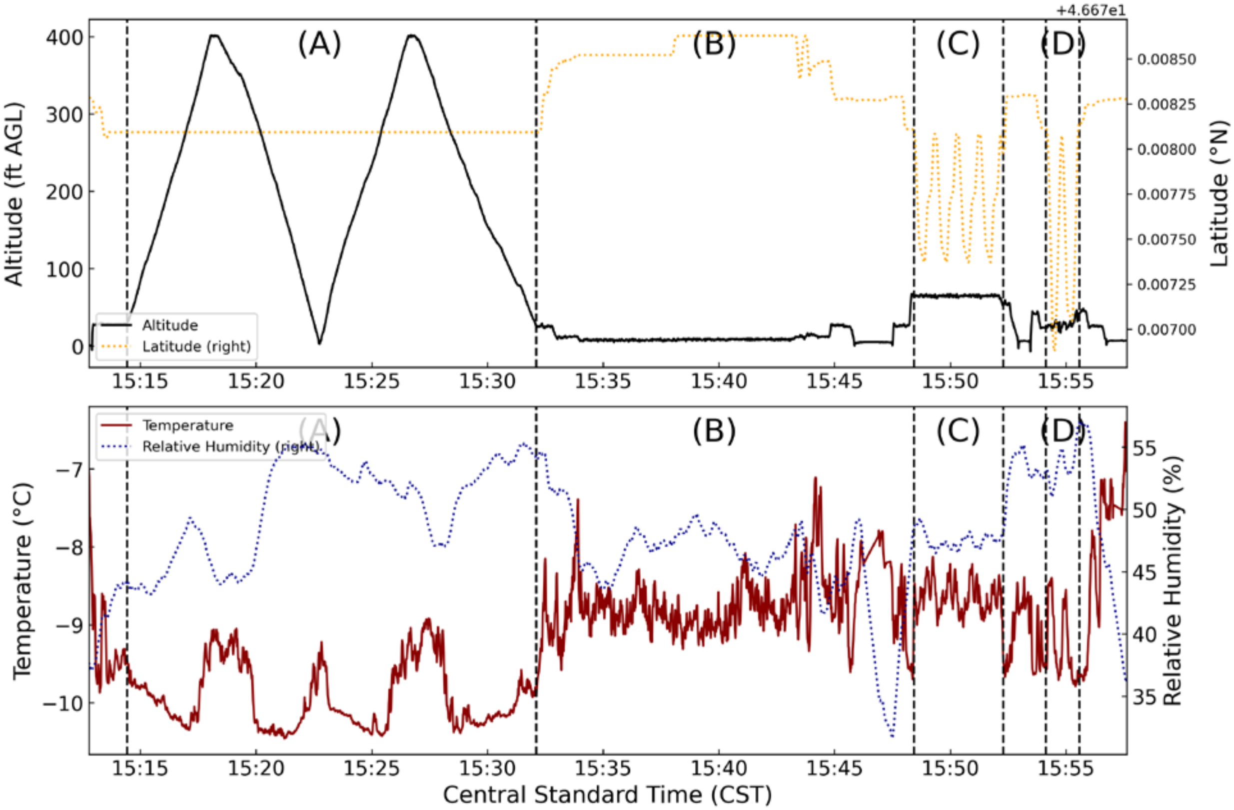

Figure 19. A representation of the March 13th, 2023 UAV flight data. The upper panel displays altitude (solid black line) on the primary y-axis and latitude (dotted orange line) on the secondary y-axis. The bottom panel displays temperature (dark red solid line) on the primary y-axis and relative humidity (dotted blue line) on the secondary y-axis. The latitude is centered at 46.67828 °N with observed changes occurring on a minute scale. Vertical black dotted lines separate four distinct maneuvers. A represents two vertical profiles. B represents a hovering period. Both C and D represent separate racetrack maneuvers.

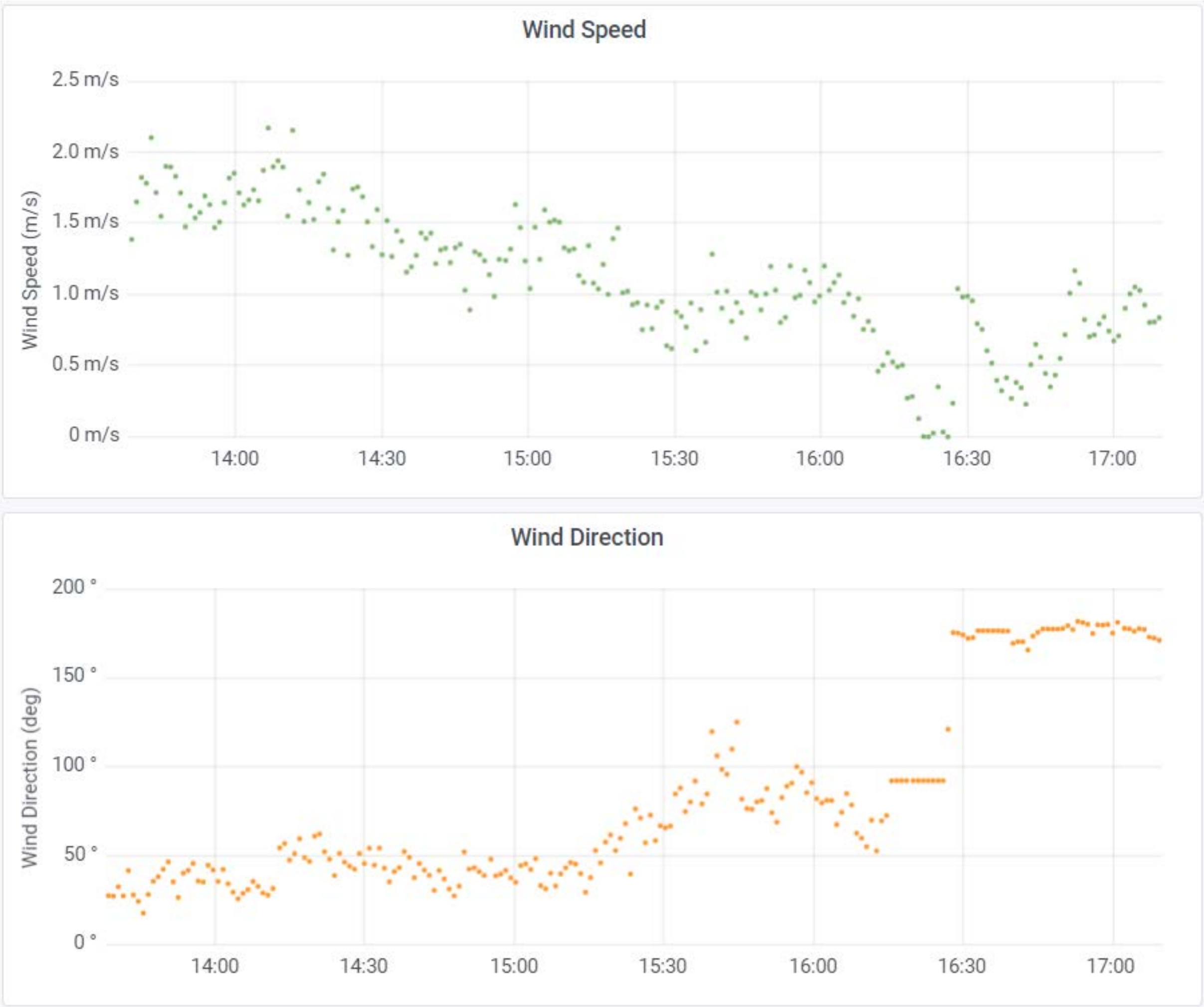

Figure 20. A panel of plots representing tripod wind speed and wind direction time series recorded by the Young Anemometer on March 13th, 2023. Data is visualized through the Grafana open-source software dashboards. All times are reported in central standard time. The UAV mission occurred between 15:12 CST and 15:58 CST.

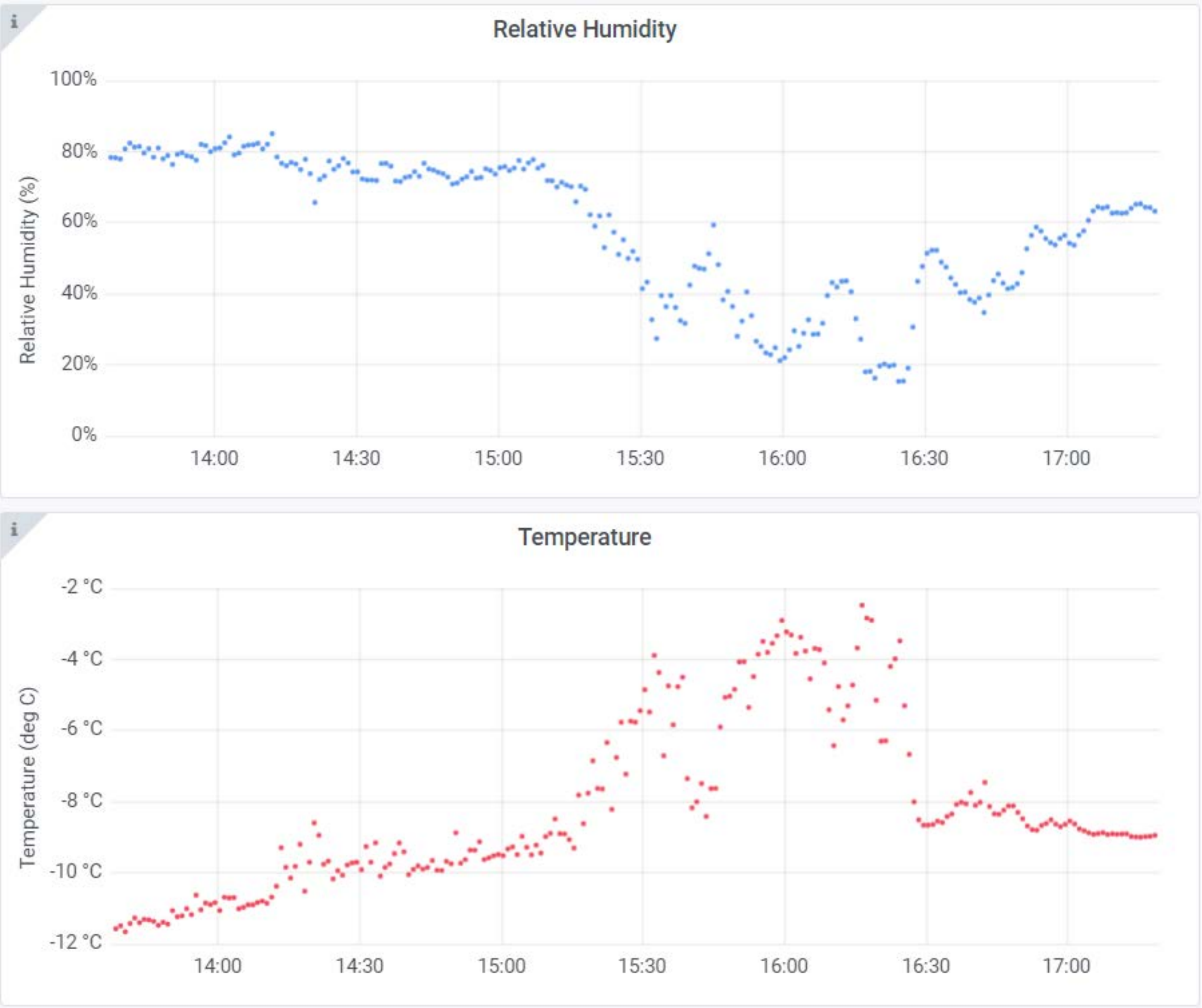

Figure 21. *A panel of plots using the same format as Figure 20, except with relative humidity and temperature time series plots recorded by the IMet-XQ2.*

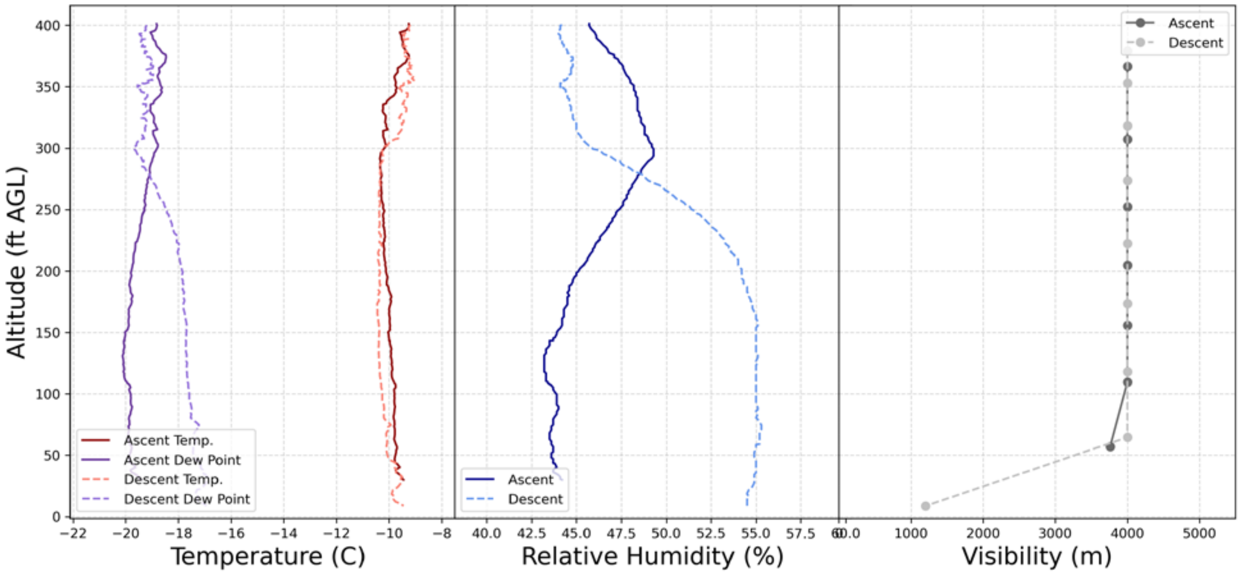

Figure 22. A panel of plots representing temperature (red), dew point (purple), relative humidity (blue), and visibility (gray) during the first March 13th, 2023 vertical profiling maneuver represented by A on Figure 19. The ascent occurred between 15:14:26 CST and 15:18:03 CST. The descent occurred between 15:18:21 CST and 15:22:42 CST.

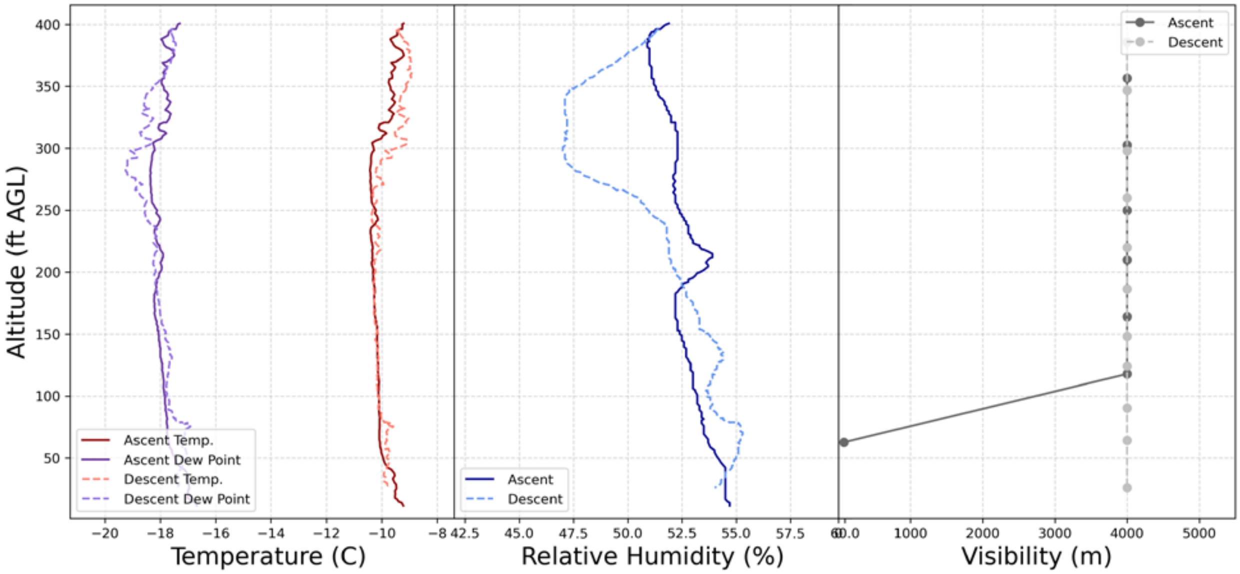

Figure 23. A panel of plots using the same format as Figure 22, but the second vertical profile represented within A on Figure 19. The ascent occurred between 15:22:50 CST and 15:26:36 CST. The descent occurred between 15:27:00 CST and 15:32:07 CST.

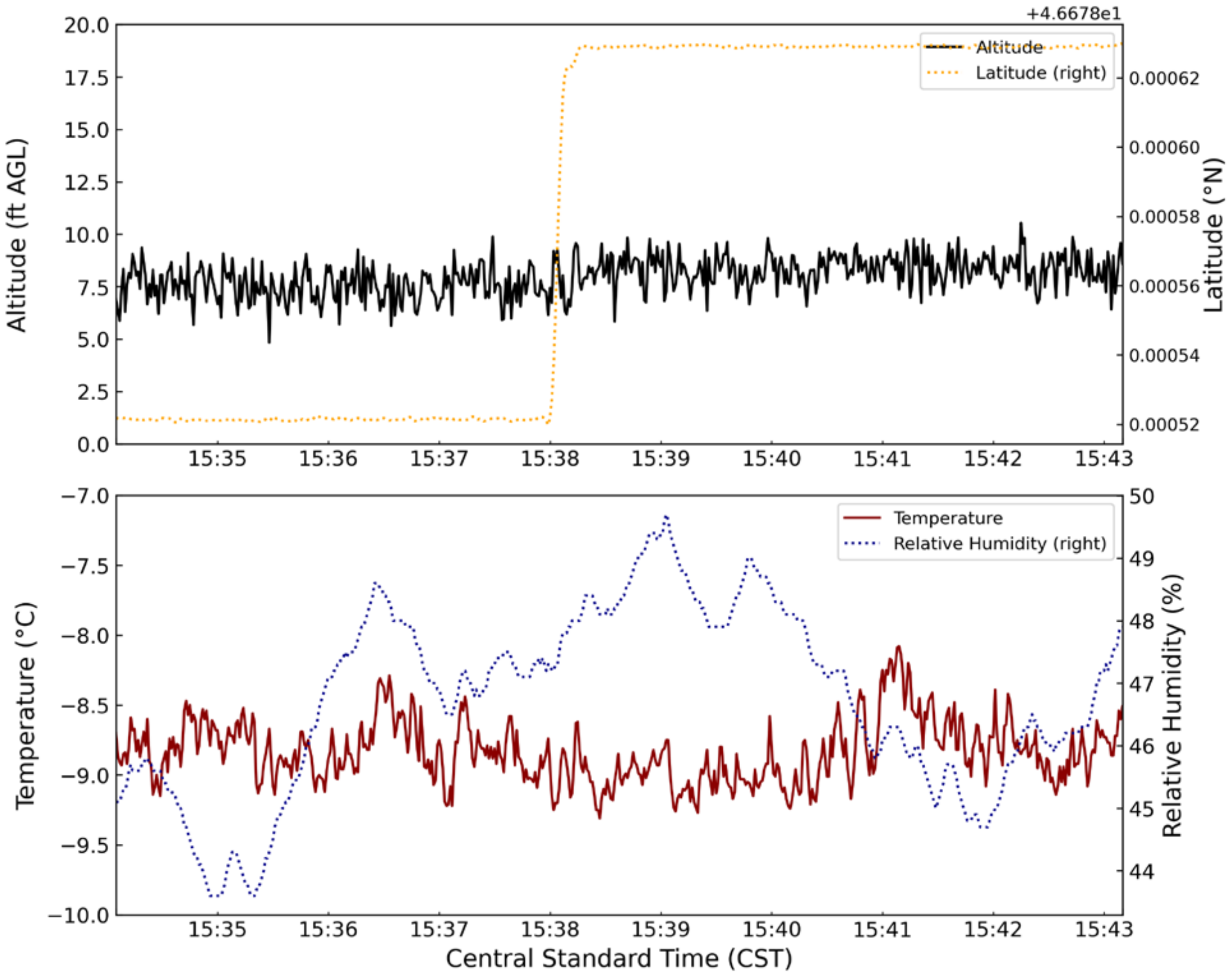

Figure 24. A panel of plots representing the UAV hovering maneuver represented by B on Figure 19. The maneuver begins at 15:34:04 CST and ends at 15:43:16 CST.

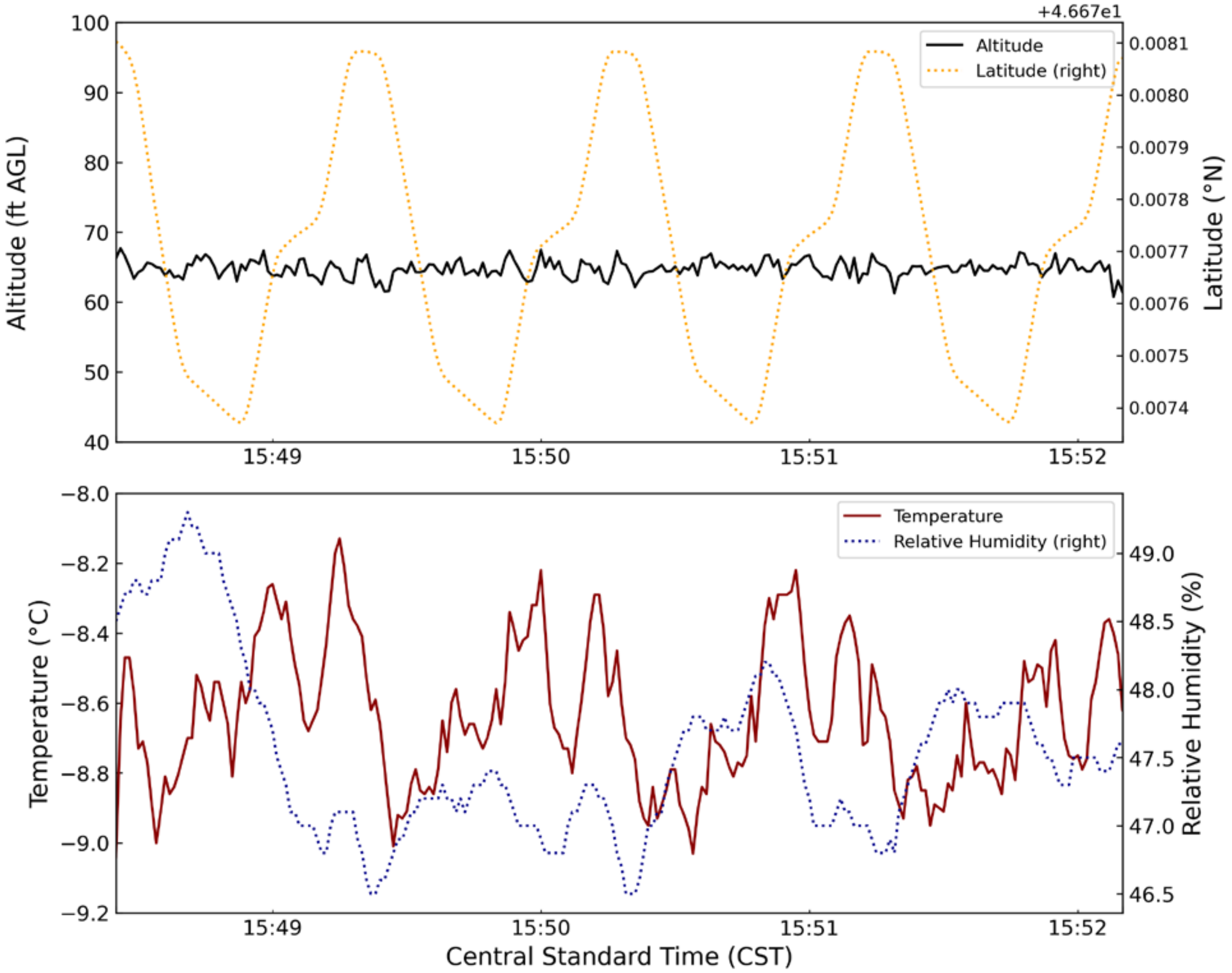

Figure 25. A panel of plots representing the UAV racetrack maneuver represented by C in Figure 19. The maneuver begins at 15:48:26 CST and ends at 15:52:10 CST.

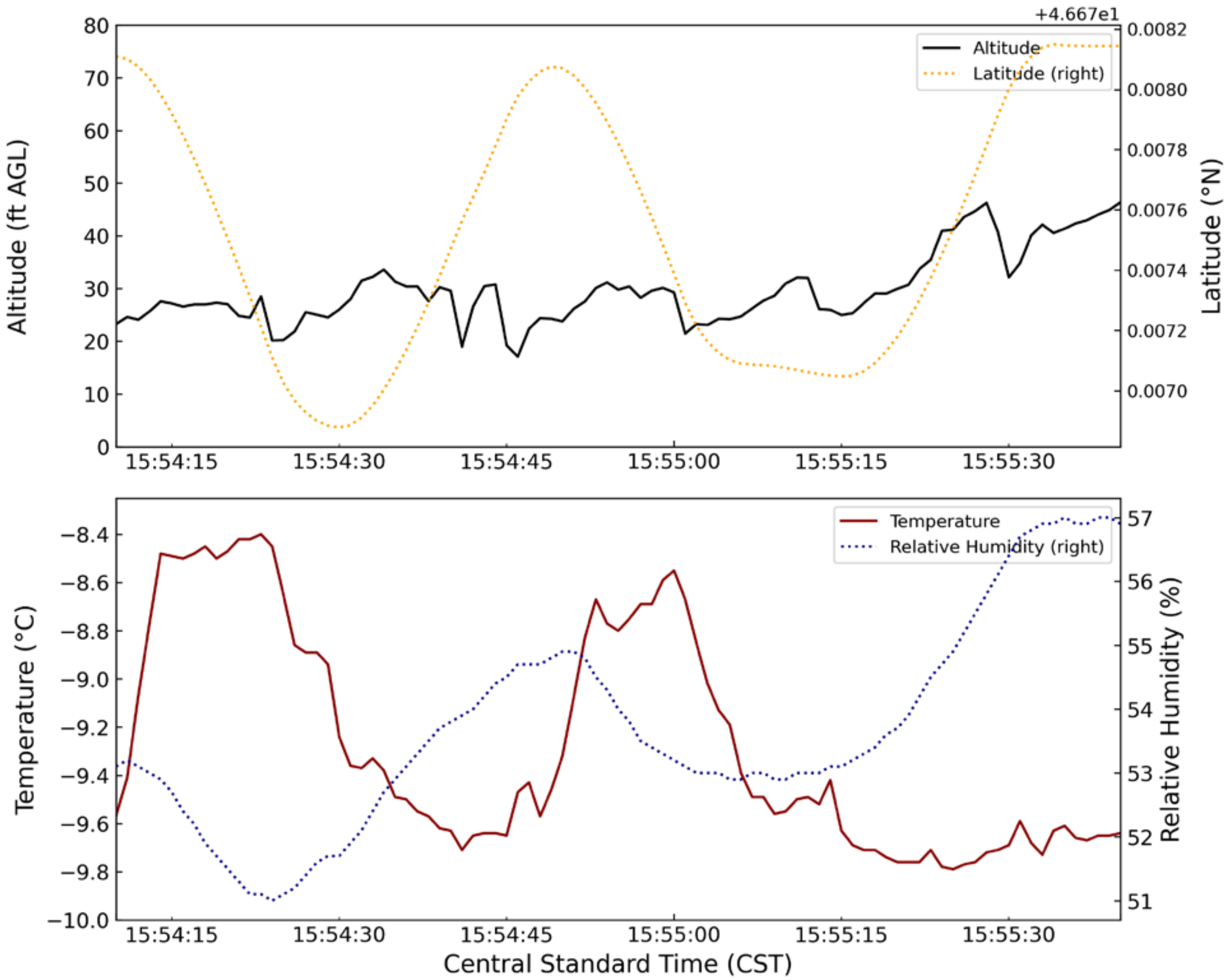

Figure 26. A panel of plots representing the UAV racetrack maneuver represented by D in Figure 19. The maneuver begins at 15:54:08 CST and ends at 15:55:35 CST.

March 15th 2023

Efficient radiational cooling and light winds allowed for periods of radiation fog to develop during the overnight and early morning hours on March 15th, 2023. The tripod MiniOFS visibility sensor registered periods of lowered visibilities by 07:40 CST (Figure 27), reaching a minimum of 316 m at 07:42:30 CST and 08:07:30 CST. The UAV was powered on and airborne by 08:06:59 CST (Figure 28). Two vertical profiling maneuvers commenced between 08:07:28 CST and 08:23:46 CST. The UAV was grounded shortly thereafter due to icing buildup concerns at 08:24:45 CST. After evaluation, the UAV was deemed airworthy, and power was reactivated by 08:27:01 CST. Brief UAV calibration maneuvers were performed before approval for a hover maneuver was granted between 08:34:00 CST and 08:45:56 CST. Two more vertical profiling maneuvers commenced thereafter between 08:46:32 CST and 08:56:37 CST. The UAV was powered down at 08:56:55 CST resulting in a total mission length of 49 minutes and 56 seconds.

While all UAV instrumentation were operational upon initial powerup, the IMet-XQ2 quickly failed due to moisture buildup from the ambient air and aided by UAV downwash. As such, UAV temperature and humidity measurements were not available for the mission. Visual confirmation of the fog was limited to a shallow diffuse layer just above the surface, supported by the return to 4000 m visibilities shortly after mission commencement (Figure 27). Surface temperatures fluctuated between -10 °C and -12 °C with relative humidities at 100 percent. Wind speeds less than 0.5 m/s resulted in a static wind direction for extended durations. Due to the shallow nature of the fog, vertical profiles failed to pick up visibility reductions outside of near-surface measurements related to ground obstruction. However, the extended hovering maneuver near 47 ft AGL recorded a gradual lowering of visibilities to 1500 m (Figure 29). UAV performance and response was deemed adequate by the pilot, with noticeable icing buildup on the propellers by mission end.

Figure 27. A panel of plots using the same format as Figure 16, except representing the March 15th 2023 UAV mission. The mission began at 08:07 CST and ended at 08:57 CST.

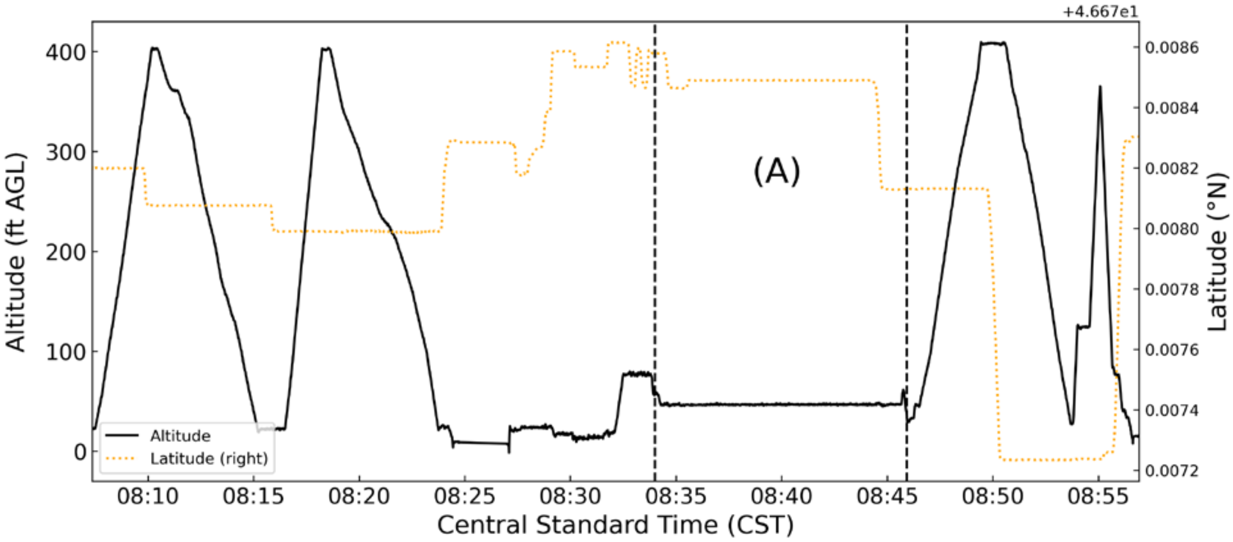

Figure 28. A plot representing the March 15th 2023 UAV flight data. Altitude (solid black line) is displayed on the primary y-axis and latitude (dotted orange line) displayed on the secondary y-axis. The latitude is centered at 46.67828 °N with observed changes occurring on a minute scale. Dotted vertical black lines represent the start and end times for the hovering maneuver designated as A.

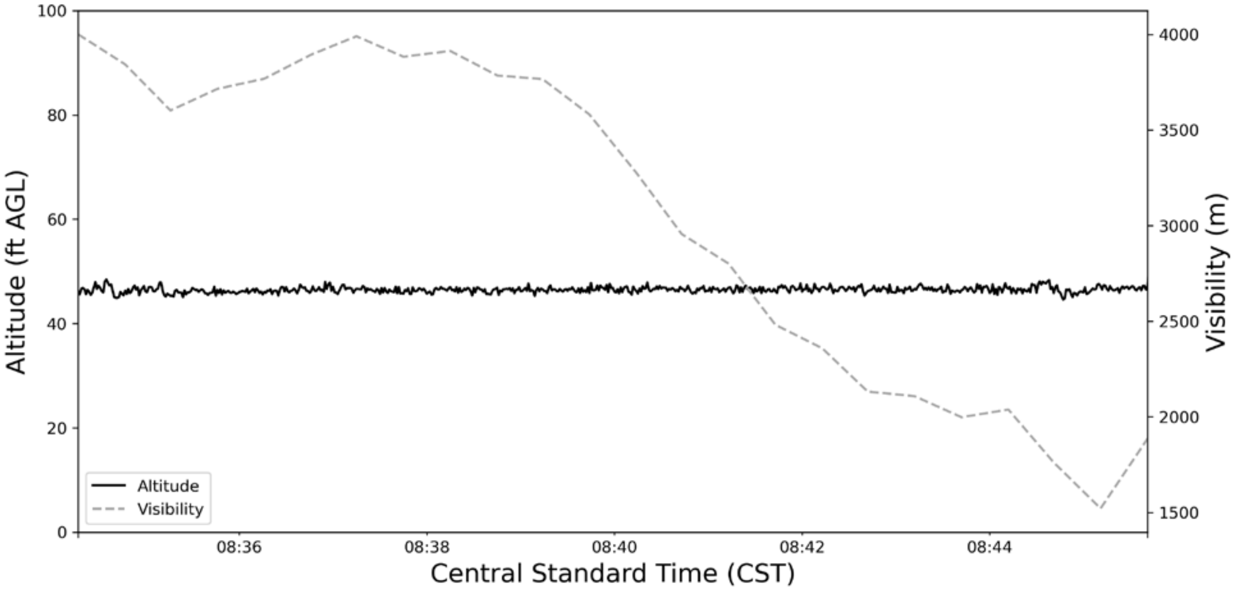

Figure 29. A plot representing the hovering maneuver as indicated by A in Figure 28. Altitude (solid black line) is represented on the y-axis and visibility (dashed gray line) is represented on the secondary y-axis.

March 23rd 2023

Surface high pressure was paired with strong upper-level ridging over the eastern Dakotas and western Minnesota on March 23rd, 2023. Light winds and clear skies allowed for efficient radiational cooling overnight, resulting in periods of dense fog throughout the Red River Valley by morning hours. Surface visibility measurements at the tripod recorded early morning instances of fog at 00:33 – 01:00 CST, 05:50 – 06:27 CST, and 07:10 – 07:27 CST (Figure 30). The first of two UAV flights began at 08:17:01 CST (Figure 31). An opaque layer of fog was observed just above the surface, obstructing views of the top half of nearby pine trees. One vertical profiling maneuver was completed between 08:19:56 CST and 08:26:17 CST. Icing buildup on the drone instigated a precautionary landing at 08:28:44 CST. The UAV was deemed airworthy after a short inspection and subsequently airborne by 08:29:31 CST. The second vertical profiling maneuver occurred between 08:30:22 CST and 08:37:28 CST. Icing buildup was more significant, and another precautionary landing occurred at 08:38:14 CST. After a longer inspection and ice removal, the UAV was airborne by 08:43:12 CST. A third vertical profiling maneuver occurred between 08:45:30 CST and 08:49:54 CST. With depleted batteries, the UAV was grounded by 08:52:07 CST. After battery replacement, the second UAV flight began at 09:13:19 CST (Figure 32). Fog was noticeably thicker and extended down to the surface by mission start. A fourth vertical profiling maneuver occurred between 09:16:21 CST and 09:27:20 CST. Noticeable ice crystals began falling out of the fog layer. The pilot noticed battery voltage issues and the UAV was grounded by 09:30:28 CST, resulting in a total mission length of 1 hour, 13 minutes and 27 seconds.

Similar to the mission on March 15th, moisture contamination rendered the IMet-XQ2 inoperable immediately after UAV power activation. As such, no temperature or humidity measurements were available. Tripod temperatures at mission start hovered around -18 °C, slowly rising to -15 °C by mission end (Figure 30). Winds remained light and never increased beyond 1.5 m s^{-1}. Consistent with visual observations of a slightly elevated fog layer, tripod visibilities measured 4000 m through the first three vertical profiling maneuvers. As fog increased in extent, tripod visibilities dipped close to 500 m at the time of the fourth vertical profile around 09:16 CST (Figure 30). A comparison of the vertical profiles in Figure 33 shows progressively lowered visibility throughout the column and a deepening fog layer. All vertical profiling maneuvers started above 20 ft AGL to avoid ground contamination for the UAV MiniOFS. While icing buildup occurred through each profiling maneuver, no noticeable drop in performance was observed by the pilot.

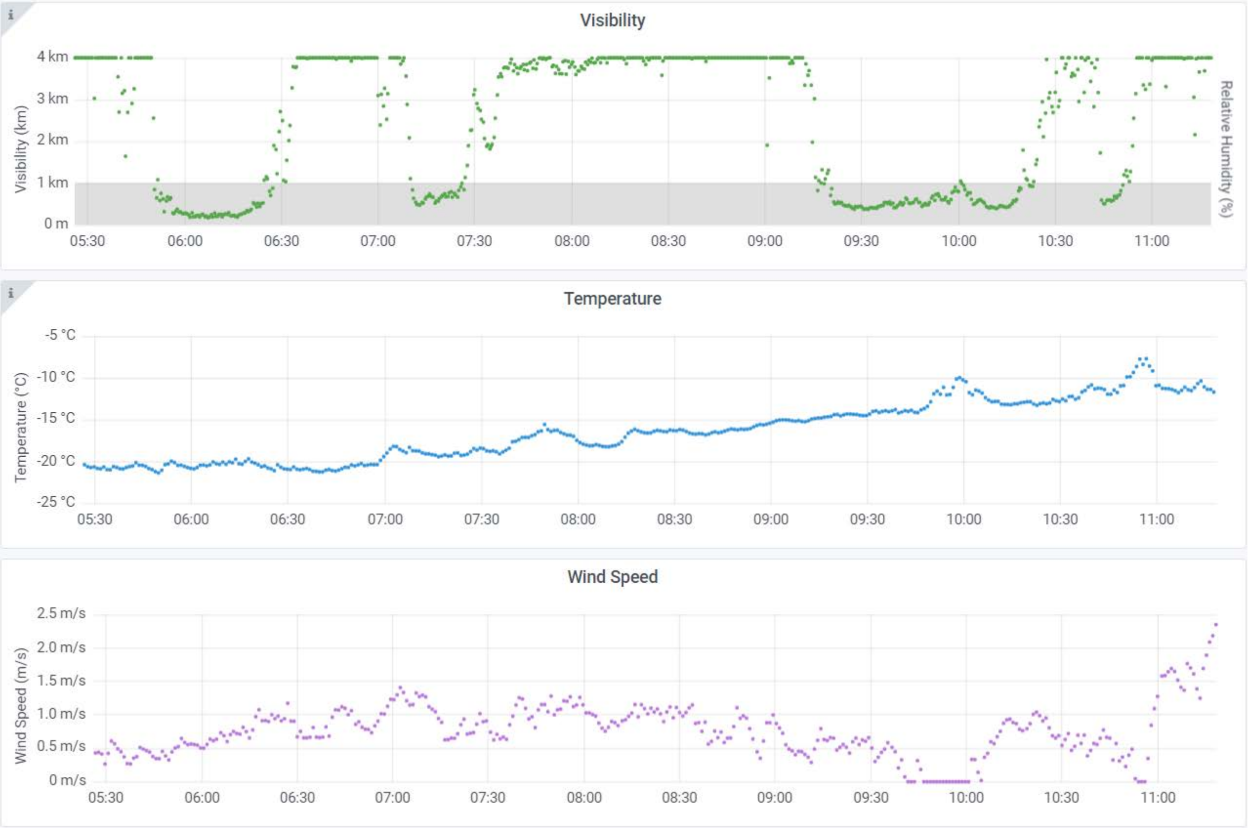

Figure 30. A panel of plots using the same format as Figure 16, except representing the March 23rd 2023 UAV mission. The mission began at 08:17 CST and ended at 09:30 CST.

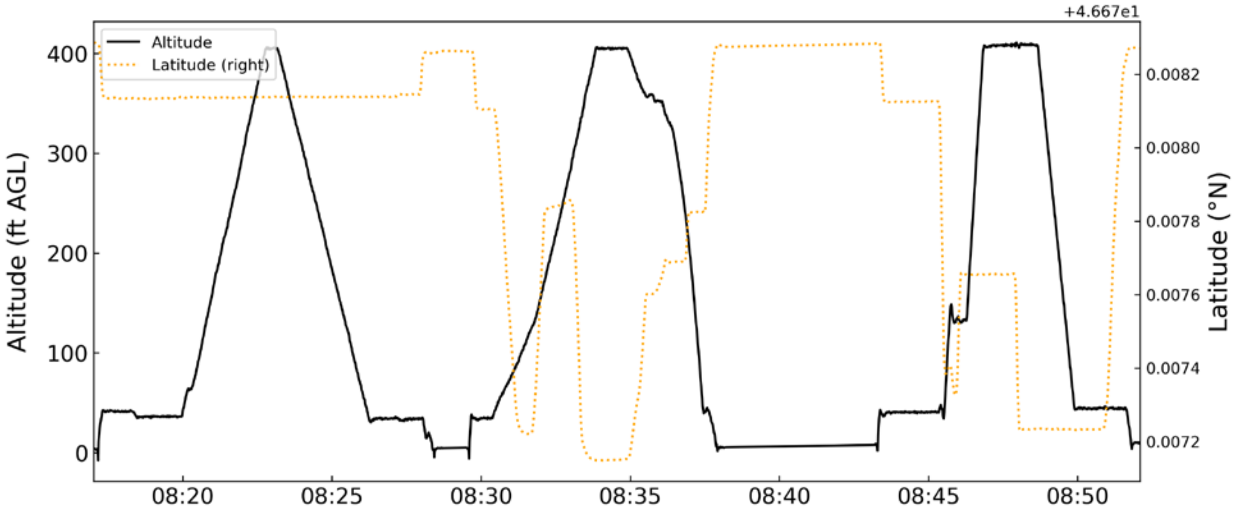

Figure 31. A plot using the same format as Figure 28, but representing the first flight of the March 23rd 2023 mission.

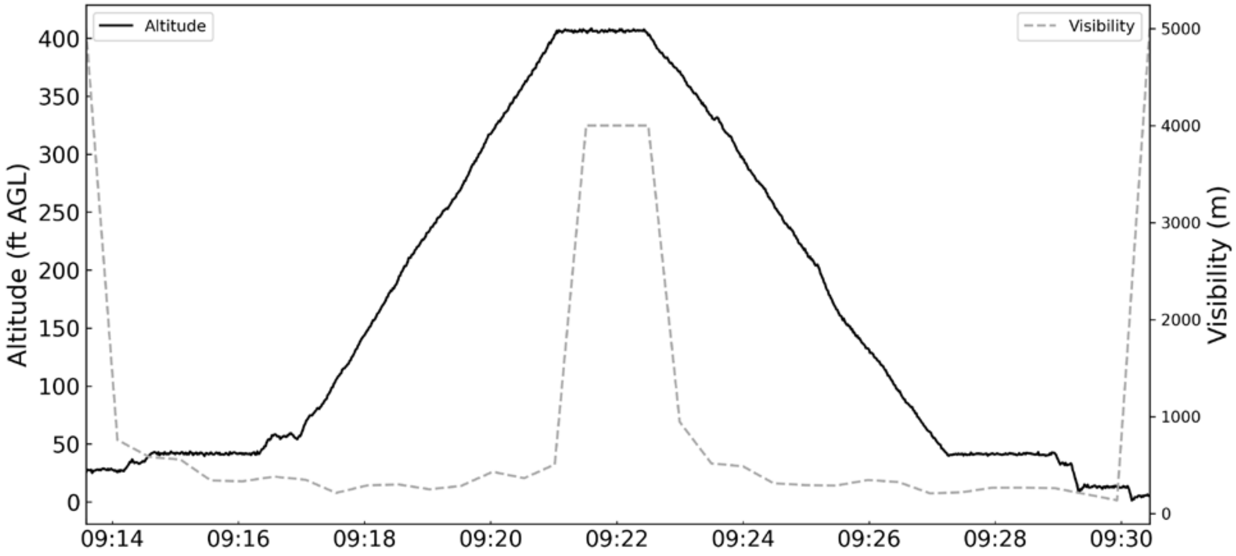

Figure 32. A plot using a similar format to Figure 31 but representing the second flight of the March 23rd 2023 mission. Altitude (black solid line) is displayed on the y-axis and visibility (gray dotted line) is displayed on the secondary y-axis.

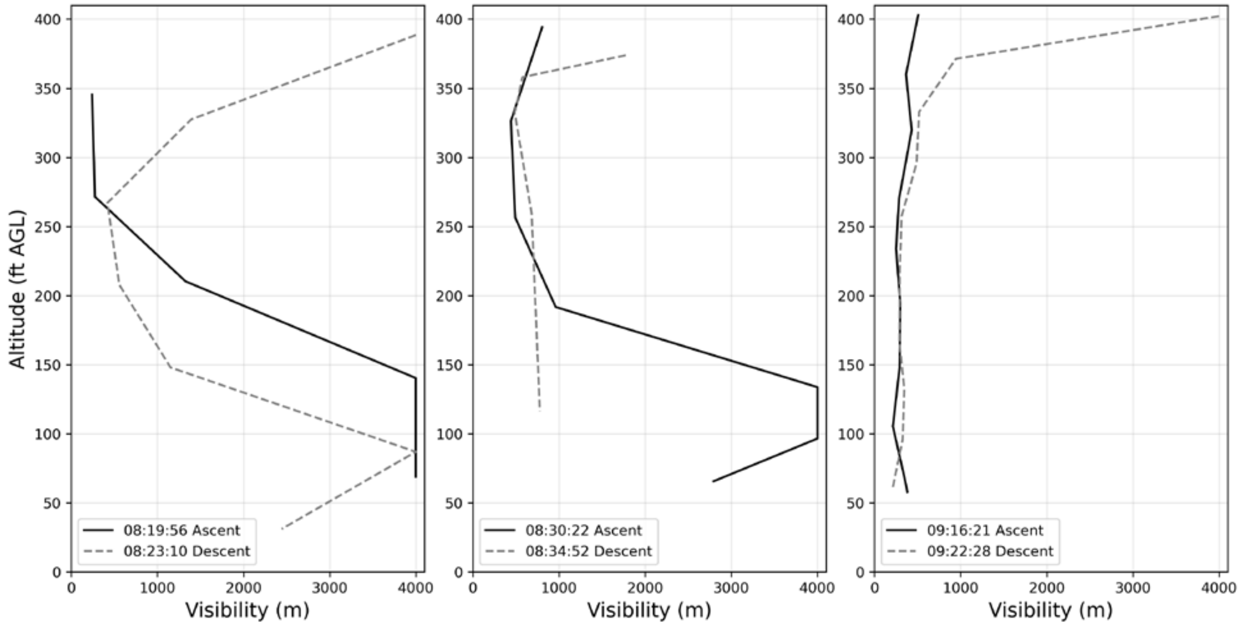

Figure 33. A three-panel representation of the first (left), second (center), and fourth (right) vertical profiling maneuvers during the March 23rd, 2023 UAV mission. For each panel, altitude is on the y-axis and visibility is the x-axis. All ascents are represented as solid black lines, and all descents are labeled as dashed gray lines. Times represented are start times for the respective maneuver in central standard time.

March 24th 2023

Surface high pressure moved to the east over Minnesota and the Great Lakes by the morning of March 24th, 2023. Compared to the previous morning, conditions for fog development were less favorable due to decreasing subsidence and ridging aloft. However, radiational cooling and clear skies were enough to initiate scattered radiation fog within the Red River Valley by the early morning hours. Surface visibility measurements from the tripod dipped below 4000 meters and hit a minimum of 1100 m by 07:25 CST (Figure 34). The UAV was airborne by 08:01:09 CST and commenced a vertical profiling maneuver from 08:02:26 CST to 08:09:27 CST (Figure 35). Fog was optically shallow and elevated, observed to obstruct the tops of nearby pine trees. After a brief landing to check on minimal icing buildup at 08:09:45 CST, a second vertical profiling maneuver commenced at 08:13:50 CST. The ascent was characterized by 50-75 ft rises followed by a 30-45 second hovering to allow a proper sampling period for the MiniOFS at each elevation.

The ascent ended at 08:22:47 CST with the following descent finished at 08:25:30 CST. The UAV powered down at 08:25:47 CST, marking a total mission length of 24 minutes and 38 seconds.

To prevent moisture contamination to the IMet-XQ2, a change in the orientation and housing of the instrument resulted in temperature and humidity measurements throughout the mission. The elevated nature of the fog is seen in both the 4000 m visibility measurements of the surface-based tripod (Figure 34) and the lowered visibilities within both vertical profiling maneuvers centered around 150 – 200 ft AGL (Figs. 36, 37). Ice crystal fallout occurred through the entirety of the UAV mission. There is a noticeable sharp decrease in temperatures coinciding at and just above the top of the visibility reductions. Ascent relative humidities are about 10 percent higher than descent relative humidities. Whereas ascent temperatures are about 2 – 3 °C colder than the descent temperatures. In the second ascent profiling maneuver, there is some variation in temperature and humidity during the hovering periods. Even so, there is a good correlation between the two ascents and between the two descents.

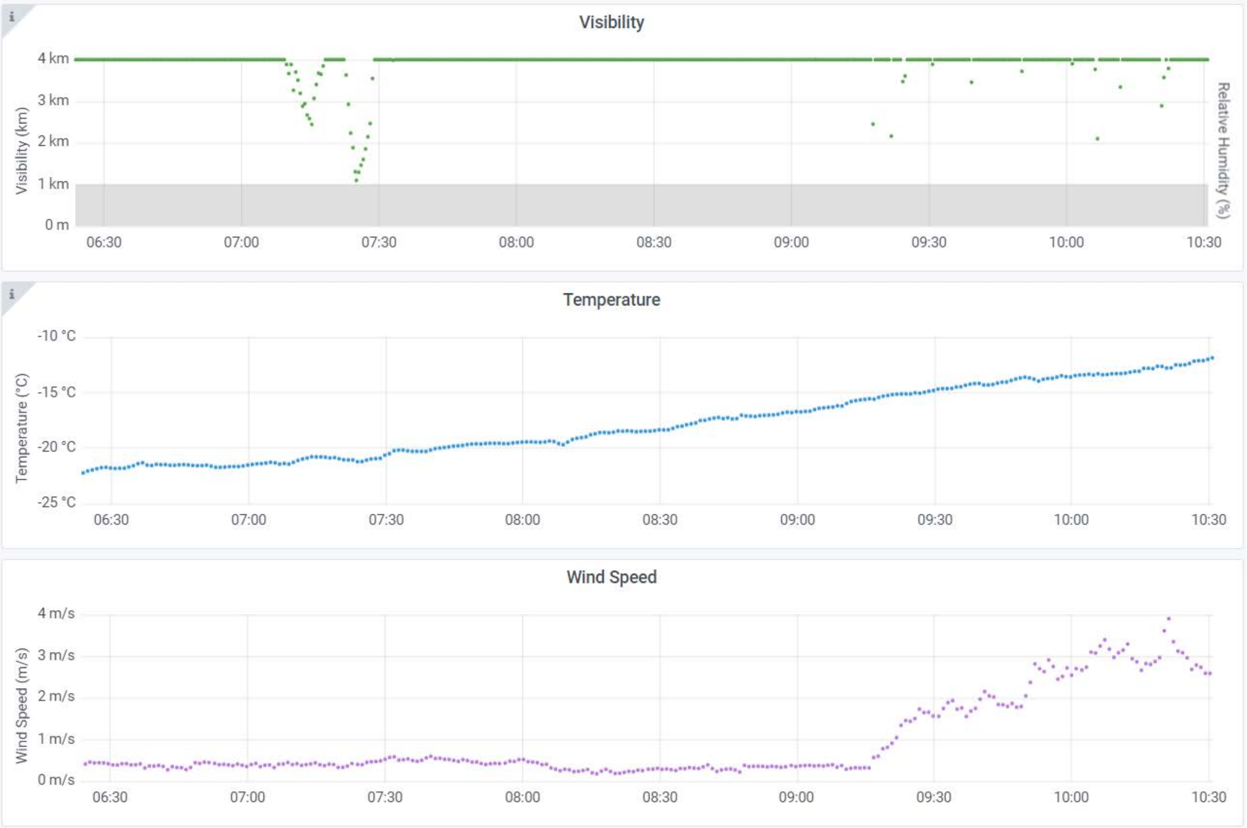

Figure 34. A panel of plots using the same format as Figure 16, except representing the March 24th 2023 UAV mission. The mission began at 08:01:09 CST and ended at 08:25:47 CST.

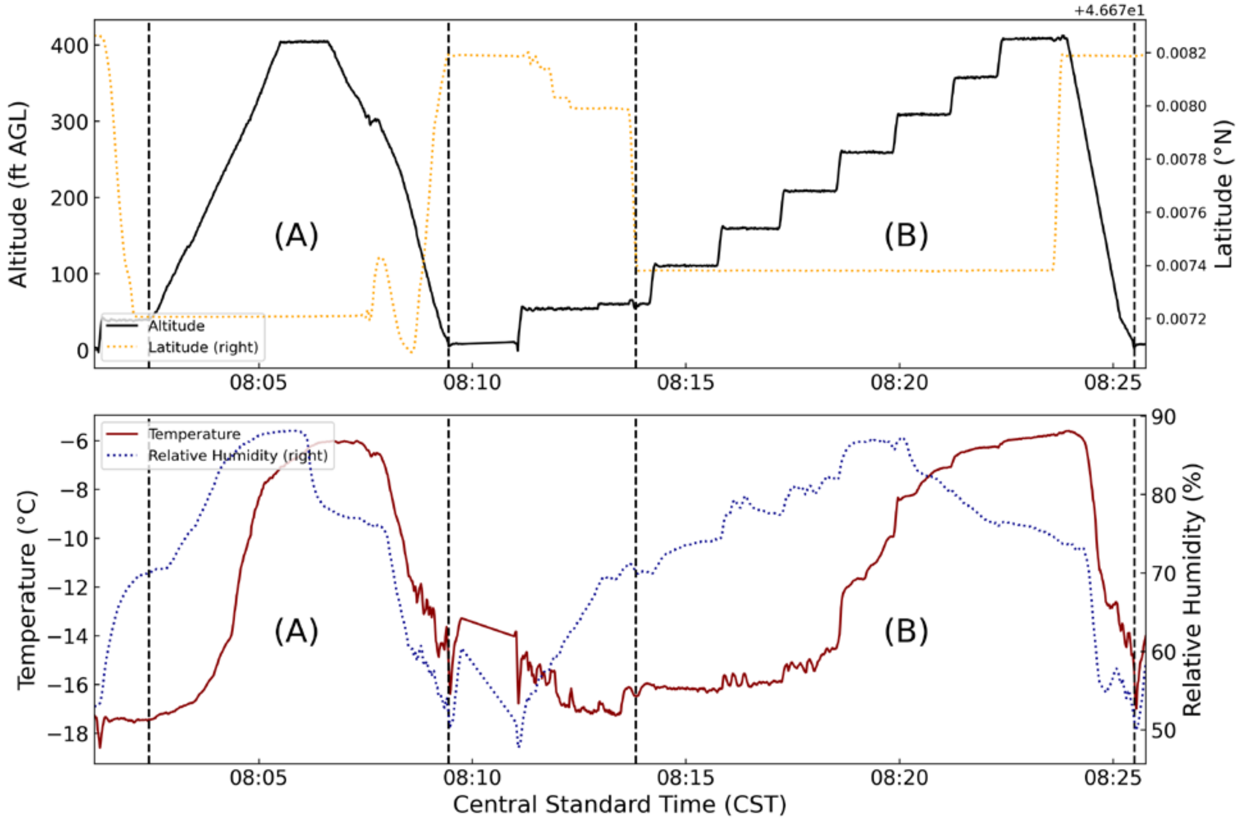

Figure 35. A panel of plots using the same format as Figure 19, but for the March 24th, 2023 mission. Vertical dashed black lines encompass the two vertical profiling maneuvers, labeled A and B.

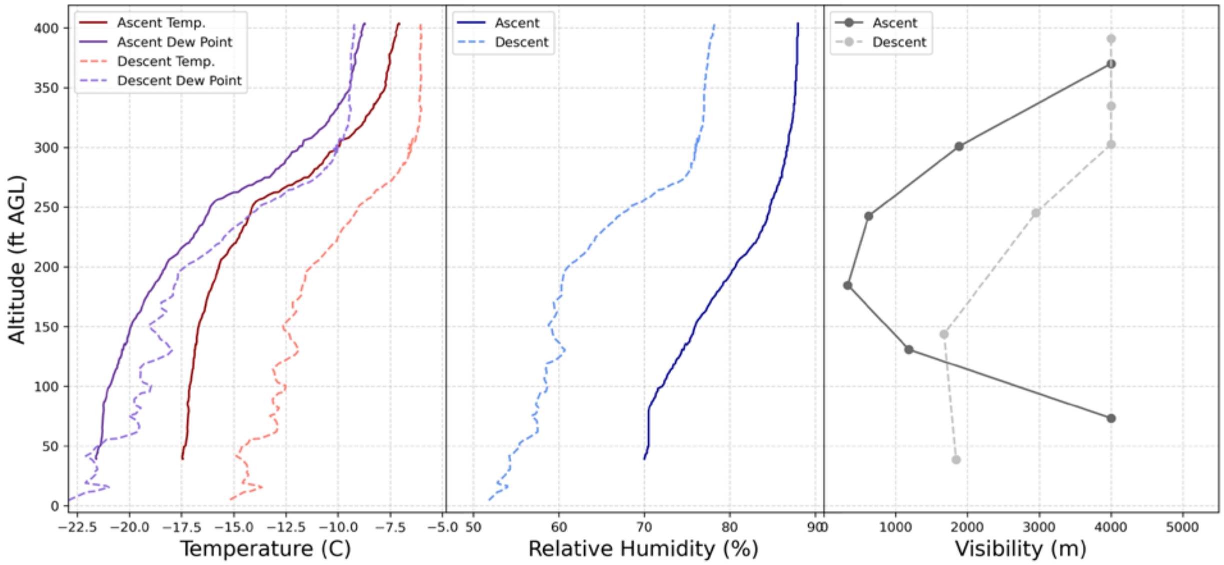

Figure 36. A panel of plots using the same format as Figure 22 but representing the first vertical profiling maneuver on March 24th, 2023, labeled A in Figure 35.

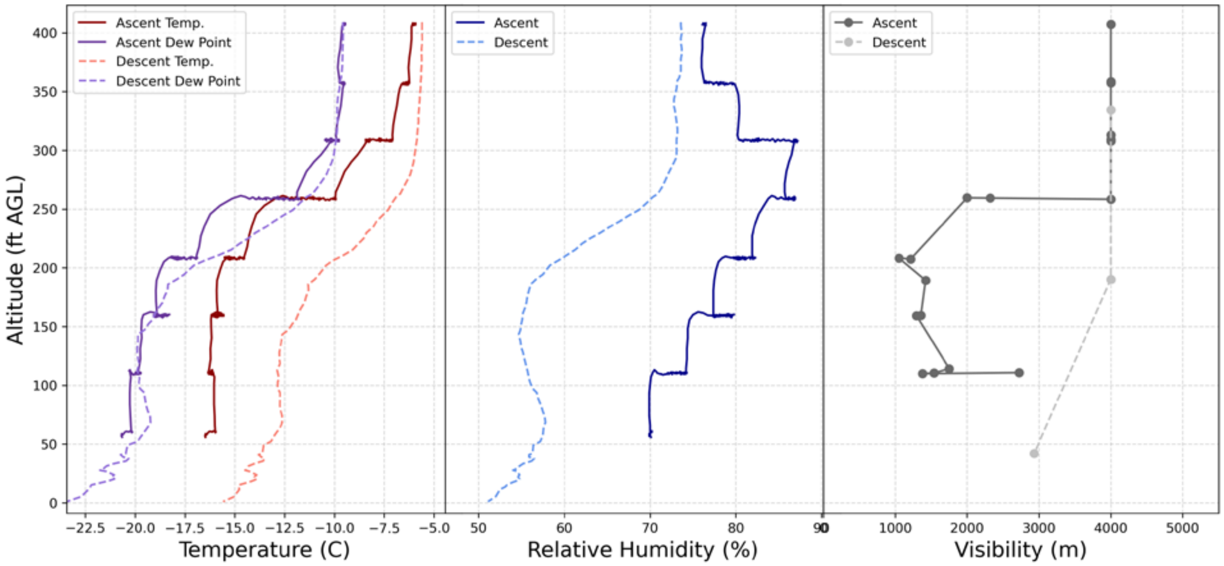

Figure 37. A panel of plots using the same format as Figure 22 but representing the second vertical profiling maneuver on March 24th, 2023, labeled B in Figure 35.

CHAPTER VI: DISCUSSION

Grand Forks Airport (KGFK), Hector International Airport (KFAR), and Jamestown Regional Airport (KJMS) show remarkably similar patterns in the temporal extent and magnitude of mist/fog probabilities. While KGFK and KFAR share a similar geographic location along the Red River, KJMS lies to the west of the Red River Valley and at a higher elevation (Figs 7, 8). This implies that the low-elevation terrain within the Red River Valley has no appreciable beneficial effect on mist/fog potential; favorable synoptic-scale setups for regional radiation fog plausibly dominate. The Red River Valley is seemingly too flat and expansive to instigate valley-inversion radiation fogs that typically require narrower valleys and sharper gradients in adjacent terrain. KRDR displayed noticeably lower probabilities within each applied threshold relative to KGFK, KFAR, and KJMS but shared the same trends in temporal extent. With all three other stations in comparative agreement, this underreporting is likely due to ASOS obstruction algorithm issues related to the inherent sensor capabilities at the KRDR site.

Seasonal and diurnal cycles in mist and/or fog probabilities are evident across all ASOS stations. The daily hourly periods of maximum probabilities coincide with the well-studied bias of fog development during the early morning hours. This morning trend shifts seasonally with the length of daytime; the earliest hours (3 – 5 CST) of maximum probability during the longer summer days and latest hours (7 – 9 CST) during the shorter winter days. The strong wintertime bias in fog potential displayed in Figure 8 appears to be significantly contaminated by blowing snow events that the ASOS obstruction algorithm fails to distinguish. The sharp cutoff in fog probabilities at the beginning of April and temporal 'banding' of higher probabilities during the winter months indicate reoccurring long-duration low-visibility events. Once a 10 m s^{-1} wind speed threshold is applied, the banding and sharp cutoff disappear almost entirely (Figure 10). While a wintertime bias in potential is still visually evident, it is subtle and negligible compared to the diurnal early morning bias.

As expected for the northern plains, supercooled mist/fog probabilities are confined to the middle of October through the beginning of April (Figure 11). The greatest probabilities are correlated to the early morning hours of February and March. Not coincidentally, this is concurrent with seasonal snowmelt in the northern Great Plains. The injection of meltwater into thawing soils aids in the process of fog development, resulting in an increased potential for surface visibility reductions. While these trends are observed within all ASOS stations, it is most enhanced at KGFK and KFAR where seasonal flooding from the nearby Red River is a yearly occurrence.

To quantify the amount of fog and/or mist occurrences the Red River Valley experiences over a year, Table 6 displays rates of yearly occurrence at KGFK by dividing the total observed hourly occurrences by the 30 years of the climatological study, organizing the results through temperature, wind, and present weather type thresholds. Each year, there are on average 129 occurrences of mist and/or fog where a 10 m s^{-1} wind threshold is applied. If the wind threshold is lowered to 5 meters per second, the occurrence rate per year drops to 53. If only instances of supercooled fog are recorded using a 5 m s^{-1} wind threshold, there are on average 14 reported occurrences of supercooled fog per year at KGFK. The substantial decreases of occurrence rate with lower wind speed thresholds suggests that blowing snow events may still be contaminating the ASOS obstruction algorithm at wind speeds below 10 m s^{-1}. However, a 5 m s^{-1} threshold is likely sufficient for filtering these events and advective fog scenarios with ambient winds between 5 and 10 m s^{-1} is plausible.

Table 6: A table representing average yearly mist and/or fog occurrences recorded by KGFK. Wind speed thresholds are represented on the rows and both temperature and present weather type are represented on the columns. "FG" is the code for fog and "BR" is the code for mist.

KGFK	**"FG" and/or "BR"**		**"FG" only**	
	All	**≤ 0 °C**	**All**	**≤ 0 °C**
≤ 10 m/s	129	61	80	37
≤ 7.5 m/s	88	41	54	24
≤ 5.0 m/s	53	24	32	14

To further aid in visualization of seasonal patterns, Figure 38 displays a histogram of total fog occurrences through the 30 yr climatological analysis, grouped by calendar day with an applied 10 m s^{-1} wind threshold. 20 day rolling averages across all ASOS stations emphasize late February through the end of March as the climatological bullseye for fog occurrences. Secondary smaller maximums occur during August through early September (warm fogs), and November through early December (cold fogs). Implementing a 0 °C threshold (Figure 39), supercooled fog occurrences begin in early November and end by the beginning of April, peaking during the month of March. This further highlights the seasonality identified in the heatmaps and successfully displays potential operational periods for UAS fog dispersal operations in the Red River Valley.

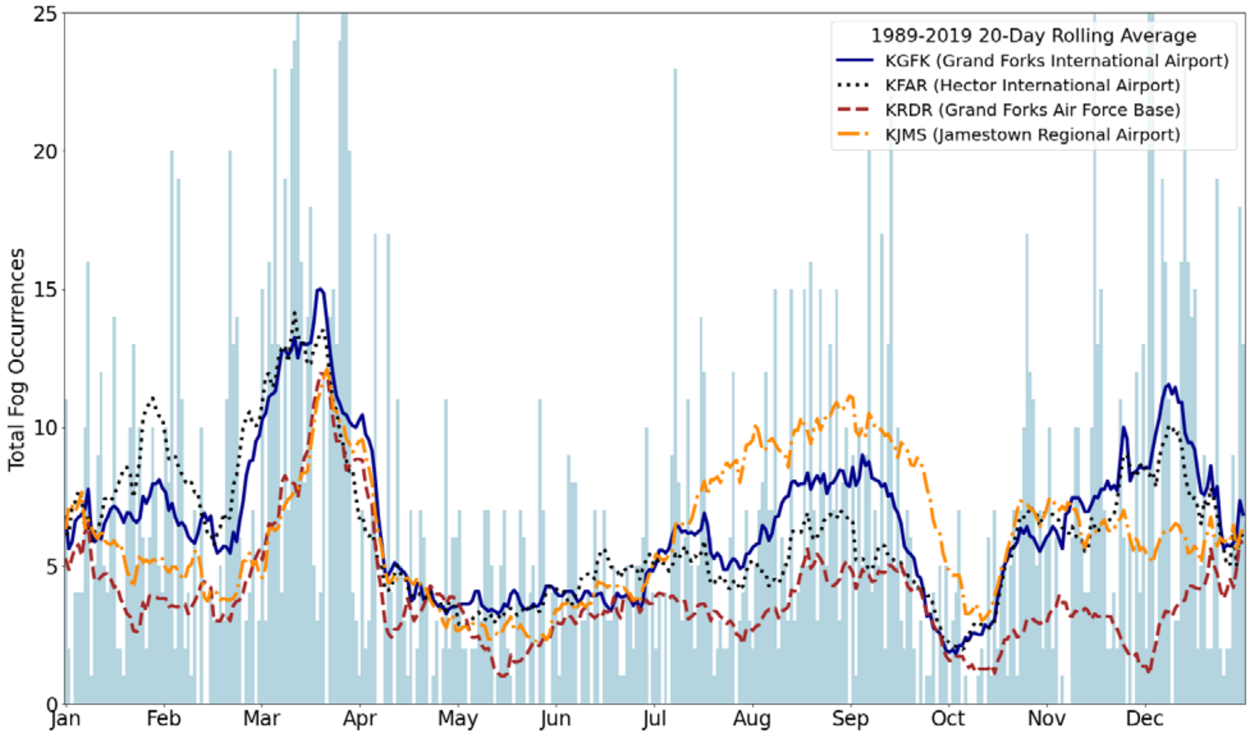

Figure 38. A plot representing the total hourly fog occurrences for the 1989-2019 climatological sampling period below a 10 m s^{-1} *threshold, grouped by calendar day and visualized through 20 day rolling averages for each station. The light blue histogram is of KGFK for reference.*

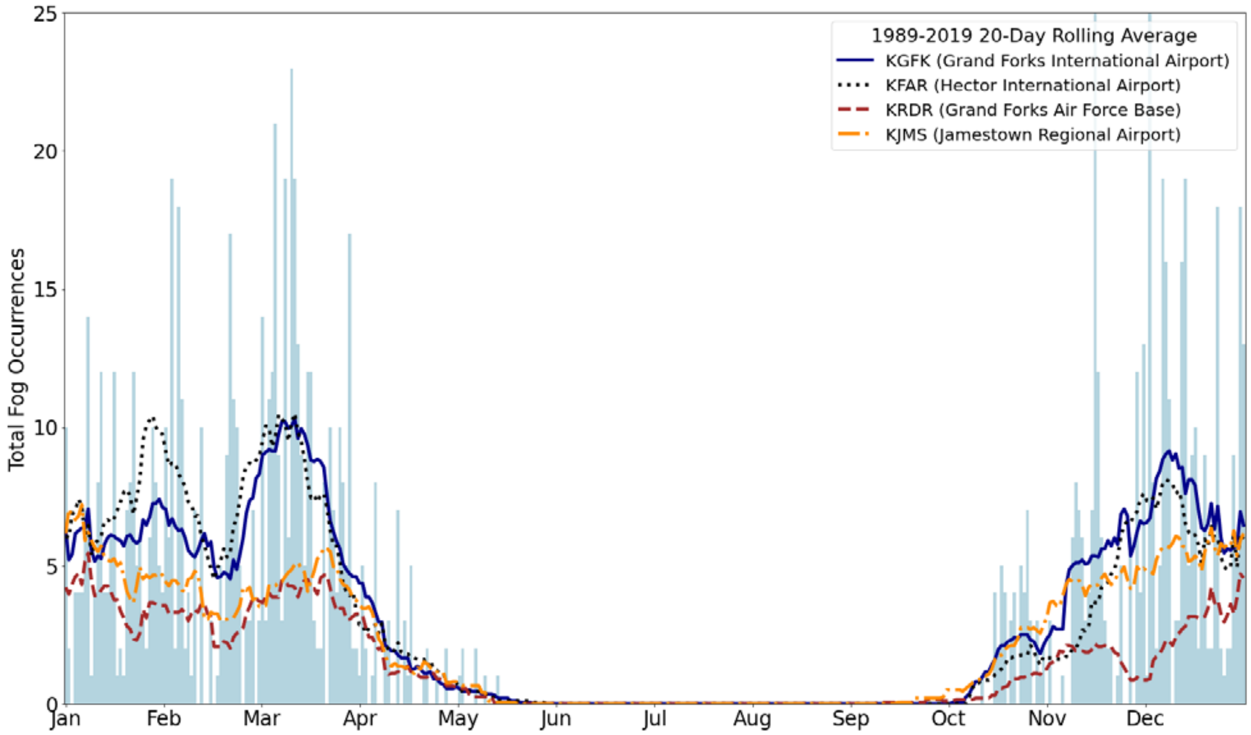

Figure 39. A plot with the same format as Figure 38 but with a ≤ 0 °C threshold.

The IMet-XQ2 temperature sensor displays a high degree of accuracy in relation to the CS125 and WXT536 temperature sensors; demonstrated by r^2-values near 1.0 and a one-to-one ($\hat{\beta}_1 \approx 1$) relationship (Figure 12). A tight clustering of the residuals demonstrates a high degree of precision for both sensor comparisons. While the IMet-XQ2 relative humidity sensor displays r^2-values above 0.95, $\hat{\beta}_1$ values less than 1.0 indicate that the sensor consistently underestimates relative humidities compared to the CS125 and WXT536 (Figure 13). This is especially apparent at higher relative humidities, where CS125 and WXT536 relative humidities near 100 percent correlate with IMet-XQ2 relative humidities that never increase above 90 percent. Radiation shielding around the IMet-XQ2 may have prevented sufficient aspiration to the relative humidity sensor and caused errors in estimation. There is a tighter clustering of residuals at lower relative humidities (less than 40 percent) compared to higher relative humidities (greater than 60 percent) for both sensor comparisons. The MiniOFS visibility measurements struggled to correlate linearly with the CS125 using a 4-kilometer ($r^2 = 0.646$) threshold. However, no fog occurred during the sampling period. Linear regressions during a fog event displayed increased correlation between the sensors. At the lowest visibilities however, correlation decreases and the MiniOFS substantially overestimates visibility compared to the CS125. This suggests a nonlinear relationship between the two sensors below 4000 m visibilities.

The tripod's platform of instrumentation provided vital surface-based observations during UAS operations and served as a source of long-term observations at ICE headquarters during the project. Internet access, and subsequent remote access to the Rasbperry Pi 4B computer, allowed for efficient monitoring of dataflow and software debugging during times of maintenance. This also helped distinguish power outages at Ice Crystal Engineering headquarters and malfunctions related to hardware. Visualization on the Grafana open-source software interface allowed for real-time monitoring of various atmospheric phenomena, most notably blowing snow/blizzards and fog. Coupled with visual confirmation via the Raspberry Pi 4B camera module, the decision-making process for UAS missions was resolutely enhanced.

The tripod platform's usage was not without difficulties. Moisture contamination from snow was a long-standing issue during the winter months that took numerous retrofits to be properly addressed. A lack of efficiently sealed openings allowed wind-blown hydrometeors to travel inside the camera box housing and short the Raspberry Pi 4B computer in multiple incidents. Power fluctuations and outages at Ice Crystal Engineering headquarters affected the operational capacity of the tripod, with manual reconnection with the power source almost always required to restart the Raspberry Pi 4B. Icing events were particularly damaging to the platform, especially for the MiniOFS optical sensor. Visibility measurements were drastically reduced until ice gradually melted off or was removed. Finally, while the two-meter height of the tripod supported identification of numerous fog events, layers of shallow fog just above the surface during the March 15th and 23rd missions were missed entirely.

The UAV platform functioned as intended for all five flight missions and in full capacity during both low and high visibility conditions. Efficient UAV calibration and startup procedures often led to mission start times shortly after the designated 08:00 CST daybreak threshold. Two flight times of 45 minutes and 49 minutes overperformed the 30-minute estimates for the four lithium-ion batteries. Swapping of the drained batteries resulted in minimal periods of mission downtime. While supercooled/ice fog missions accrued substantial ice buildup during the March 23rd and 24th fog missions, no noticeable performance degradation was observed by the licensed pilot. Outside of minor shorting issues within the internal electrical system while grounded, no UAV platform issues arose during flights.

Temperature and relative humidity profiles exhibited high resolutions of the lower boundary layer and illustrated the robustness of the IMet-XQ2 one-second sampling rates. IMet-XQ2 sensor response times at very cold temperatures (around -10 °C) generated a considerable downward shift of the descent profiles compared to the ascent profiles for both the temperature and relative humidity sensors. This was particularly evident during the March 7th profiling maneuver where 10-20 ft differences in the ascent and descent were observed (Figure 22). As suggested by the IMet-XQ2 regression analysis, bigger discrepancies arose with the relative humidity measurements, at times producing 10-20 percent differences between the ascents and descents on March 15th and 24th. Relative humidities never increased above 90 percent during any fog mission. However, similar discrepancies were evident in the more precise temperature sensor on March 24th with a noticeable 2-5 °C warm bias for descents (Figure 36Figure 37). This could be a combination of issues related to heat contamination from the UAV body, turbulent mixing of the atmospheric column via UAV downwash, and sensor response times. Proper housing of the IMet-XQ2 further and horizontally away from the UAV body is recommended to help mitigate these issues. Additionally, racetrack patterns exhibited cyclical responses in the temperature and humidity sensors, suggesting speed and direction biases for the IMet-XQ2.

Visibility was successfully profiled by the MiniOFS during the March 23rd and March 24th fog missions. A deepening fog layer during the March 23rd mission is evident in the vertical profiles; visibilities decreased throughout the atmospheric column with each subsequent profiling maneuver (Figure 33). Importantly, the top of the fog layer was encountered between 350 and 400 ft AGL as indicated by increasing visibilities. Similar features were evident during the elevated fog mission on March 24th, however the entire fog layer between 100 and 300 ft AGL is profiled (Figure 36 and Figure 37). This is supported by a strong inversion present in the IMet-XQ2 temperature measurements directly at and above the top of reduced visibilities. The second ascent maneuver with interspersed 30-45 s hovering periods helped alleviate issues related to the 30 s MiniOFS sampling rate and allowed for better vertical resolution.

Efforts to determine the feasibility of a supercooled fog abatement project within the Red River Valley accomplished numerous objectives. Production of a regional supercooled fog climatology displayed seasonal potential beginning in early November, peaking during the month of March, and ending by the beginning of April. Acquisition of FAA-approved airspace for low-visibility UAS platform usage resulted in successful tests of the platform in both low and high visibility conditions, demonstrating functionality of the UAV in icing conditions. Attached instrumentation succeeded in representing the boundary layer during clear-air and foggy conditions, indicating successful in-situ data acquisition using the UAS platform. The important fog-top identification for fog dispersal methods occurred during two of the low-visibility missions.

The ground-based platform acted sufficiently as verification of surface conditions during UAS platform missions. Overall, tests of the UAS platform for supercooled fog abatement demonstrate clear potential and favorability for operational usage.

Nevertheless, numerous issues need to be addressed for an accurate determination on the feasibility of such a supercooled fog dispersal project within the Red River Valley. There are clear indications from the regional fog climatologies that the ASOS obscuration algorithm does not precisely filter all snow/blowing snow events and is highly dependent on the functionality of the precipitation sensor. At the lowest wind speed thresholds, small amounts of average hourly supercooled fog conditions per year suggest low occurrence rates and cast doubt on a monetary benefit in Red River Valley supercooled fog dispersal operations. Outside of a general seasonal outlook, continued ASOS investigation and additional sources of data for the data-sparse Red River Valley is necessary for a more precise fog climatology. Areas west of the Red River Valley where sharper gradients in terrain result in increased valley-inversion fog potential may prove more suitable for supercooled fog abatement endeavors.

CHAPTER VII: SUMMARY AND CONCLUSIONS

A research study was conducted to explore the efficacy of the UAS platform in acquiring fog microphysical data and determine the feasibility of a supercooled fog dispersal project in the Red River Valley. A 30 yr fog climatology for the Red River Valley indicates a seasonal period for supercooled fog development from early November through the beginning of April, peaking sharply during the month of March coincident with yearly snowmelt. Secondary maximums in fog occurrence probabilities during August-September (warm fogs) and late November-December (cold fogs) are plausibly related to favorable synoptic-scale setups for regional radiation fogs. The Red River Valley does not display a marked increase in fog potential compared to the surrounding terrain, largely due to the expansive flat nature of the valley. Overall low hourly averages of supercooled fog occurrences per year cast some doubt onto the monetary feasibility of such a supercooled fog abatement project within the Red River Valley itself.

The UAS platform demonstrated clear and favorable potential for in-situ data acquisition and operational usage during fog abatement endeavors, culminating in five successful days of test flights. High-resolution vertical profiles of temperature and relative humidity demonstrate the robustness of the IMet-XQ2 sampling rate. However, numerous discrepancies between the ascent and descent patterns for both IMet-XQ2 sensors indicate UAV-related aspiration and heat contamination issues that need to be addressed. The setup of the IMet-XQ2 underneath the main body likely experienced heat contamination during vertical profiling maneuvers and particularly for ascents. Furthermore, sensor response times produce a substantial shift between the ascents/descents and must be corrected/calibrated post-mission for an accurate representation of the boundary layer. Visibility was successfully profiled by the MiniOFS during clear-air and foggy conditions, however the 30 second sampling rate proved detrimental to representative sampling outside of hovering and low-speed maneuvers. Fog tops were reached during two of the fog missions, successfully demonstrating an ability to reach the critical altitude for most theoretical fog dispersal methods. Additionally, substantial icing accretion instigated little to no performance degradation of the UAV.

The UAS platform is still in its inception with regards to meteorological data acquisition; more efforts within fogs implementing the IMet-XQ2, MiniOFS, and other relevant miniaturized instrumentation is needed in future studies. Internet accessibility on the UAS platform would help with real-time data monitoring and aid in the quick identification of fog top heights critical to fog dispersal methods. Numerous failures of the IMet-XQ2 highlight the necessity of proper housing to protect instrumentation from solar and moisture contamination. Similar to work done by Islam et al. (2021), instrumentation setups further away (ideally horizontally) from the UAV body will help avoid heat contamination. Future work also includes gaining FAA approvals for seeding material utilization, nighttime operations, and operations above 400ft AGL. Finally, more fog research using alternative non-ASOS data sources is necessary for an accurate monetary determination on the feasibility of supercooled fog abatement within Red River Valley.

REFERENCES

Beckwith, W. B., 1965: supercooled fog dispersal for airport operations. *Bulletin of the American Meteorological Society*, **46**, 323–327, https://doi.org/10.1175/1520-0477-46.6.323.

Brooks, G., 2017: Red River Valley, Manitoba: The Geomorphology of a Low-Relief, Flood-Prone Prairie Landscape. 143–155.

Burn, D. H., and N. K. Goel, 2001: Flood frequency analysis for the Red River at Winnipeg. *Can. J. Civ. Eng.*, **28**, 355–362, https://doi.org/10.1139/l00-122.

Capobianco, G., and M. D. Lee, 2001: The Role of Weather in General Aviation Accidents: An Analysis of Causes, Contributing Factors and ISSUES. *Proceedings of the Human Factors and Ergonomics Society Annual Meeting*, **45**, 190–194, https://doi.org/10.1177/154193120104500241.

Chong, J., S. Lee, S. Shin, S. E. Hwang, Y. Lee, and S. Kim, 2020: Research on Meteorological Technology Development Using Rotary Multicopter Unmanned Aerial Vehicles and Its Application. *2020 International Conference on Unmanned Aircraft Systems (ICUAS)*, 2020 International Conference on Unmanned Aircraft Systems (ICUAS), 540–544.

Christensen, L. S., and W. Frost, 1980: NASA Contractor Report 3255: Fog Dispersion.

Delene, D. J., 2011: Airborne data processing and analysis software package. *Earth Sci Inform*, **4**, 29–44, https://doi.org/10.1007/s12145-010-0061-4.

Eldridge, R. G., 1971: The Relationship Between Visibility and Liquid Water Content in Fog. *Journal of the Atmospheric Sciences*, **28**, 1183–1186, https://doi.org/10.1175/1520-0469(1971)028<1183:TRBVAL>2.0.CO;2.

Garland, J. A., 1971: Some fog droplet size distributions obtained by an impaction method. *Quarterly Journal of the Royal Meteorological Society*, **97**, 483–494, https://doi.org/10.1002/qj.49709741408.

Gultepe, I., M. D. Müller, and Z. Boybeyi, 2006: A New Visibility Parameterization for Warm-Fog Applications in Numerical Weather Prediction Models. *Journal of Applied Meteorology and Climatology*, **45**, 1469–1480, https://doi.org/10.1175/JAM2423.1.

Gultepe, I., and Coauthors, 2007: Fog research: A review of past achievements and future perspectives. *Pure and Applied Geophysics*, **164**, 1121–1159.

Gultepe, I., and Coauthors, 2015: A review on ice fog measurements and modeling. *Atmospheric Research*, **151**, 2–19, https://doi.org/10.1016/j.atmosres.2014.04.014.

Gultepe, I., A. J. Heymsfield, M. Gallagher, L. Ickes, and D. Baumgardner, 2017: Ice Fog: The Current State of Knowledge and Future Challenges. *Meteorological Monographs*, **58**, 4.1-4.24, https://doi.org/10.1175/AMSMONOGRAPHS-D-17-0002.1.

Haase, J., 2007: A Climatology of LIFR Conditions in the Upper Midwest Stratified by Type of Weather.

Hicks, J. R., and G. Vali, 1973: Ice Nucleation in Clouds by Liquefied Propane Spray. *Journal of Applied Meteorology and Climatology*, **12**, 1025–1034, https://doi.org/10.1175/1520-0450(1973)012<1025:INICBL>2.0.CO;2.

Hoffmann, F., 2020: Effects of Entrainment and Mixing on the Wegener–Bergeron–Findeisen Process. *Journal of the Atmospheric Sciences*, **77**, 2279–2296, https://doi.org/10.1175/JAS-D-19-0289.1.

Houghton, H. G., and W. H. Radford, 1936: On the Local Dissipation of Natural Fog. *Physical Oceanogoraphy and Meteorology*, **6**.

Islam, A., A. Shankar, A. Houston, and C. Detweiler, 2021: University of Nebraska unmanned aerial system (UAS) profiling during the LAPSE-RATE field campaign. *Earth Syst. Sci. Data*, **13**, 2457–2470, https://doi.org/10.5194/essd-13-2457-2021.

Kennedy, A., A. Trellinger, T. Grafenauer, and G. Gust, 2019: A Climatology of Atmospheric Patterns Associated with Red River Valley Blizzards. *Climate*, **7**, 66, https://doi.org/10.3390/cli7050066.

Kimball, S. K., C. J. Montalvo, and M. S. Mulekar, 2020: Assessing iMET-XQ Performance and Optimal Placement on a Small Off-the-Shelf, Rotary-Wing UAV, as a Function of Atmospheric Conditions. *Atmosphere*, **11**, 660, https://doi.org/10.3390/atmos11060660.

Korolev, A., 2007: Limitations of the Wegener–Bergeron–Findeisen Mechanism in the Evolution of Mixed-Phase Clouds. *Journal of the Atmospheric Sciences*, **64**, 3372–3375, https://doi.org/10.1175/JAS4035.1.

Kroft, P. J., J. R. Holton, J. A. Curry, and J. A. Pyle, 2003: *Encyclopedia of atmospheric sciences*. Academic Press, 2780 pp.

Kunkel, B. A., 1984: Parameterization of Droplet Terminal Velocity and Extinction Coefficient in Fog Models. *Journal of Applied Meteorology and Climatology*, **23**, 34–41, https://doi.org/10.1175/1520-0450(1984)023<0034:PODTVA>2.0.CO;2.

Lease, J. C., and C. S. Zeigler, 1972: Doing Away with Fog. *The Military Engineer*, **64**, 258–261.

Leung, A. C. W., W. A. Gough, and K. A. Butler, 2020: Changes in Fog, Ice Fog, and Low Visibility in the Hudson Bay Region: Impacts on Aviation. *Atmosphere*, **11**, 186, https://doi.org/10.3390/atmos11020186.

Liu, D. Y., W. L. Yan, J. Yang, M. J. Pu, S. J. Niu, and Z. H. Li, 2016: A Study of the Physical Processes of an Advection Fog Boundary Layer. *Boundary-Layer Meteorol*, **158**, 125–138, https://doi.org/10.1007/s10546-015-0076-y.

Liu, Q., B. Wu, Z. Wang, and T. Hao, 2020: Fog Droplet Size Distribution and the Interaction between Fog Droplets and Fine Particles during Dense Fog in Tianjin, China. *Atmosphere*, **11**, 258, https://doi.org/10.3390/atmos11030258.

Liu, X. Y., 2000: Heterogeneous nucleation or homogeneous nucleation? *The Journal of Chemical Physics*, **112**, 9949–9955, https://doi.org/10.1063/1.481644.

Mason, J., 1982: The Physics of Radiation Fog. *Journal of the Meteorological Society of Japan. Ser. II*, **60**, 486–499, https://doi.org/10.2151/jmsj1965.60.1_486.

Michna, P., J. Schenk, R. A. Werner, and W. Eugster, 2013: MiniCASCC — A battery driven fog collector for ecosystem research. *Atmospheric Research*, **128**, 24–34, https://doi.org/10.1016/j.atmosres.2013.02.009.

National Oceanic and Atmospheric Administration, 2019: Federal Meteorological Handbook No.1, Surface Weather Observations and Reports.

Oxtoby, D. W., 1992: Homogeneous nucleation: theory and experiment. *J. Phys.: Condens. Matter*, **4**, 7627, https://doi.org/10.1088/0953-8984/4/38/001.

Park, M.-G., H.-S. Kang, and Y.-J. Kim, 2023: A Study on the Effectiveness of SCD Seeding Fog Dissipation Mechanism Using LiDAR Sensor. *Fluids*, **8**, 185, https://doi.org/10.3390/fluids8060185.

Pruppacher, H. R., and J. D. Klett, 2010: Homogeneous Nucleation. *Microphysics of Clouds and Precipitation*, H.R. Pruppacher and J.D. Klett, Eds., *Atmospheric and Oceanographic Sciences Library*, Springer Netherlands, 191–215.

Riedl, A., Y. Li, J. Eugster, N. Buchmann, and W. Eugster, 2022: Technical note: High-accuracy weighing micro-lysimeter system for long-term measurements of non-rainfall water inputs to grasslands. *Hydrology and Earth System Sciences*, **26**, 91–116, https://doi.org/10.5194/hess-26-91-2022.

Ryznar, E., 1977: Advection-radiation fog near lake Michigan. *Atmospheric Environment (1967)*, **11**, 427–430, https://doi.org/10.1016/0004-6981(77)90004-X.

Schaefer, V. J., 1946: The Production of Ice Crystals in a Cloud of Supercooled Water Droplets. *Science*, **104**, 457, https://doi.org/10.1126/science.104.2707.457.

——, 1968: the early history of weather modification. *Bulletin of the American Meteorological Society*, **49**, 337–342.

Stolaki, S. N., S. A. Kazadzis, D. V. Foris, and T. S. Karacostas, 2009: Fog characteristics at the airport of Thessaloniki, Greece. *Natural Hazards and Earth System Sciences*, **9**, 1541–1549, https://doi.org/10.5194/nhess-9-1541-2009.

Storelvmo, T., and T. Ivy, 2015: The Wegener-Bergeron-Findeison process - Its discovery and vital importance for weather and climate. *Meteorologische Zeitschrift*,.

Vardiman, L., E. D. Figgins, and H. S. Appleman, 1971: Operational Dissipation of Supercooled Fog Using Liquid Propane. *Journal of Applied Meteorology and Climatology*, **10**, 515–525, https://doi.org/10.1175/1520-0450(1971)010<0515:ODOSFU>2.0.CO;2.

Vonnegut, B., 1947: The Nucleation of Ice Formation by Silver Iodide. *Journal of Applied Physics*, **18**, 593–595, https://doi.org/10.1063/1.1697813.

Weinstein, A. I., 1974: Projected Utilization of Warm Fog Dispersal Systems at Several Major Airports. *Journal of Applied Meteorology and Climatology*, **13**, 788–795, https://doi.org/10.1175/1520-0450(1974)013<0788:PUOWFD>2.0.CO;2.

——, 1977: Fog Dispersal: A Technology Assessment. *J. Aircraft*, **14**.

——, and B. A. Silverman, 1973: A Numerical Analysis of Some Practical Aspects of Airborne Urea Seeding for Warm Fog Dispersal at Airports. *Journal of Applied Meteorology and Climatology*, **12**, 771–780, https://doi.org/10.1175/1520-0450(1973)012<0771:ANAOSP>2.0.CO;2.

——, and J. R. Hicks, 1976: Use of Compressed Air for Supercooled Fog Dispersal. *Journal of Applied Meteorology (1962-1982)*, **15**, 1226–1231.

Willett, H. C., 1928: FOG AND HAZE, THEIR CAUSES, DISTRIBUTION, AND FORECASTING. *Monthly Weather Review*, **56**, 435–468, https://doi.org/10.1175/1520-0493(1928)56<435:FAHTCD>2.0.CO;2.

Zinke, J., and Coauthors, 2021: The development of a miniaturised balloon-borne cloud water sampler and its first deployment in the high Arctic. *Tellus B: Chemical and Physical Meteorology*, **73**, 1–12, https://doi.org/10.1080/16000889.2021.1915614.